

# Sassy Title

by

E. Ross



A thesis submitted to the  
University of Birmingham  
for the degree of  
DOCTOR OF PHILOSOPHY

Solar and Stellar Physics Group (SASP)  
School of Physics and Astronomy  
University of Birmingham  
Birmingham, B15 2TT  
Month 20XX

# Abstract

You're awesome. Make sure the examiners know it

# Acknowledgements

Who do you hate least?

# Contents

<b>1 HiSPARC as a Space Weather Detector</b>	<b>1</b>
1.1 Introduction . . . . .	1
1.2 Aims . . . . .	2
1.3 HiSPARC Properties . . . . .	2
1.4 HiSPARC Observations . . . . .	5
1.5 Air Shower Simulations . . . . .	7
1.6 Standardisation of HiSPARC Data . . . . .	11
1.7 HiSPARC Observations After Pressure Corrections . . . . .	20
1.8 Discussion . . . . .	20
<b>2 Galactic Cosmic Ray Behaviour During Solar Cycle 24</b>	<b>22</b>
2.1 Introduction . . . . .	22
2.2 Data . . . . .	28
2.3 Time-Lag Analysis . . . . .	30
2.4 Hysteresis Effect Analysis . . . . .	36
2.5 Conclusions . . . . .	41
2.6 Update: End of Cycle 24 . . . . .	43
2.7 Comparison with HiSPARC . . . . .	43
<b>Bibliography</b>	<b>44</b>

# List of Figures

1.1	Azimuthal and zenith angle variations in the allowed and forbidden rigidity trajectories for HiSPARC station 501. . . . .	4
1.2	The vertical asymptotic viewing directions of 5 HiSPARC stations. The rigidity range of the simulations were from $1.0 \text{ GV} < R < 20.0 \text{ GV}$ , and the results are plotted in geographic coordinates on January 20th 2005. The diamonds correspond to the HS ground location and the circles correspond to the AVD for a specific rigidity value. . . . .	5
1.3	HiSPARC data for stations 501 and 3001 around the epoch of GLE 70. The plot shows the minute-averaged and 5-minute-averaged trigger events between detectors within the station. The vertical red, dashed line depicts the approximate onset time of the GLE. . . . .	6
1.4	HiSPARC data for stations 8001 and 3001 around the epoch of GLE 71. The plot shows the minute-averaged and 5-minute-averaged trigger events between detectors within the station. The vertical red, dashed line depicts the approximate onset time of the GLE. . . . .	7
1.5	HiSPARC data for 4 stations around the epoch of GLE 72. The top panel of each subplot shows the minute-averaged trigger events between detectors within the station, while the bottom panel shows the mean-shifted, minute-averaged counts by each individual detector in the station. The vertical red, dashed line depicts the approximate onset time of the GLE. . . . .	8
1.6	HiSPARC data for stations 501 and 8001 around the epoch of the FD in March 2012. The plot shows the minute-averaged and hourly-averaged trigger events between detectors within the station. The vertical blue-dashed line shows the approximate onset-time of the FD. . . . .	10
1.7	HiSPARC data for stations 501 and 8001 around the epoch of the FD in July 2012. The plot shows the minute-averaged and hourly-averaged trigger events between detectors within the station. The vertical blue-dashed line shows the approximate onset-time of the FD. . . . .	10
1.8	HiSPARC data for 4 stations around the epoch of the FD in December 2014. The plot shows the minute-averaged and hourly-averaged trigger events between detectors within the station. The vertical blue-dashed line shows the approximate onset-time of the FD. . . . .	11

1.9	HiSPARC data for [n] stations around the epoch in which there were several FDs close to the onset of GLE 72. The top panel of each subplot shows the minute-averaged trigger events between detectors within the station, while the bottom panel shows the mean-shifted, minute-averaged counts by each individual detector in the station. The vertical blue-dashed lines show the approximate onset-times of the two FDs observed around this epoch and the red-dashed line depicts the approximate onset time of the GLE. . . . .	12
1.10	Mean muon density footprints for (a) proton-initiated air showers and (b) $\alpha$ -particle-initiated air showers with intial PCR trajectories with zenith angles $\theta = 0^\circ$ and various PCR energies. The error bars given represent $1\sigma$ . . . . .	13
1.11	Mean number of muons produced at ground level by the PCR for (a) proton-initiated air showers and (b) $\alpha$ -particle-initiated air showers, for various PCR energy. The uncertainty bars given represent $1\sigma$ . . . . .	13
1.12	.....	14
1.13	The barometric coefficient calculation: (a) during November 2017 for the South Pole (SOPO) NM station, (b) during November 2019 for HiSPARC station 501 at Nikhef. . . . .	15
1.14	A comparison between the monthly barometric coefficient computed in this work and using the online barometric coefficient tool throughout the year 2017 for the SOPO NM station. . . . .	16
1.15	Pressure corrected HiSPARC data for 2 stations around the epoch of GLE 71. The top panel of each subplot shows the minute-averaged trigger events between detectors within the station, while the bottom panel shows the mean-shifted, minute-averaged counts by each individual detector in the station. The vertical red, dashed line depicts the approximate onset time of the GLE. . . . .	19
1.16	Pressure corrected HiSPARC data for 2 stations around the epoch of GLE 72. The top panel of each subplot shows the minute-averaged trigger events between detectors within the station, while the bottom panel shows the mean-shifted, minute-averaged counts by each individual detector in the station. The vertical red, dashed line depicts the approximate onset time of the GLE. . . . .	19
1.17	.....	20
1.18	.....	20
1.19	Pressure corrected HiSPARC data for [n] stations around the epoch in which there were several FDs close to the onset of GLE 72. The top panel of each subplot shows the minute-averaged trigger events between detectors within the station, while the bottom panel shows the mean-shifted, minute-averaged counts by each individual detector in the station. The vertical blue-dashed lines show the approximate onset-times of the two FDs observed around this epoch and the red-dashed line depicts the approximate onset time of the GLE. . . . .	21

2.1	SSN (top), with vertical lines showing the beginning of each solar cycle. Cosmic ray intensity recorded by NMs (bottom), with vertical lines showing the approximate epochs of solar magnetic field polarity reversals. (MCMD = McMurdo, NEWK = Newark, SOPO = South Pole, THUL = Thule). . . . .	24
2.2	Hysteresis plots between yearly averaged SSN and yearly averaged GCR intensity for each of the 4 main NM stations over cycles 19-24. . . . .	26
2.3	Variation in the correlation coefficient with time-lag NM station GCR intensity and SSN during solar cycles 20-23. . . . .	31
2.4	Variation in the correlation coefficient with time-lag between NM GCR intensity and SSN during solar cycle 24. . . . .	32
2.5	Variation in the correlation coefficient with time-lag between NM GCR intensity and SSN between 2000-2012. . . . .	34
2.6	Variation in time-lag plotted against NM station rigidity cut-off for the 16 NM stations detailed in Table 2.1. . . . .	35
2.7	The hysteresis plots for even solar cycles 20 and 22 and the linear regression fit to the data. . . . .	38
2.8	The hysteresis plots for odd solar cycles 21 and 23 and the linear regression fit to the data. . . . .	39
2.9	The hysteresis plots for odd solar cycles 21 and 23 and the ellipse fit to the data. . . . .	39
2.10	The hysteresis plot for solar cycle 24, and the linear regression fit to the data (left) and ellipse fit to the data (right). . . . .	41
2.11	The monthly-mean CR-induced muon count rate recorded by HiS-PARC (blue), and the SSN (black) between 2008 – 2019. . . . .	44
2.12	. . . . .	45

# List of Tables

1.1	Properties of some of the HiSPARC stations: geographic longitude ( $\lambda$ ), geographic latitude ( $\phi$ ), altitude ( $h$ ), and the geomagnetic vertical cut-off rigidity ( $R_C$ ) calculated from the PLANETOCOSMICS simulations. . . . .	4
1.2	Space weather events investigated within the HiSPARC data. The percentage change column provides a reference of how much the CR counts observed by the NM station at Oulu ( $R_c=0.81$ GV) increased or decreased by, due to the space weather event. . . . .	6
1.3	PCRs simulated using CORSIKA. . . . .	9
2.1	Neutron monitor stations used in this study and their vertical geomagnetic cut-off rigidity ( $R_c$ ), longitude, latitude, and altitude acquired from NEST. The first four stations have been used for all of the analysis while the lower 12 stations have been used exclusively for the investigation into the dependence of $R_c$ on the time-lag. . . . .	29
2.2	Time-lags and the corresponding cross-correlation coefficient between NM CR count and SSN for solar cycles 20-23. . . . .	32
2.3	Time-lags and the corresponding cross-correlation coefficient between NM GCR intensity and SSN for solar cycle 24. . . . .	32
2.4	Time-lags and the corresponding cross-correlation coefficient between NM GCR intensity and SSN during 2000-2012. . . . .	34
2.5	Correlation coefficients of the linear regression and ellipse modeling of the hysteresis plots for solar cycles 20-23. . . . .	37
2.6	Correlation coefficients of the linear regression and ellipse modeling of the hysteresis plots for solar cycle 24. . . . .	40



# Abbreviations

ADC	Analogue to Digital Converter
AS	Air Shower
AVD	Asymptotic Viewing Direction
BiSON	Birmingham Solar Oscillations Network
CMA	Central Moving Average
CME	Coronal Mass Ejection
CR	Cosmic Ray
EAS	Extensive Air Shower
EV	Enhanced Variance
FD	Forbush Decrease
FE	Forbush Effect
FOV	Field Of View
GCR	Galactic Cosmic Ray
GIC	Ground Induced Current
GLE	Ground Level Enhancement
GMDN	Global Muon Detector Network
GNSS	Global Navigation Satellite System
GZK	Greisen-Zatsepin-Kuzmin
HCS	Heliospheric Current Sheet
HiSPARC	High School Project on Astrophysics and Research with Cosmics
ICME	Interplanetary Coronal Mass Ejection
IMF	Interplanetary Magnetic Field
LC	Loss Cone
MD	Muon Detector
MFP	Mean Free Path
MIP	Minimum Ionising Particle
MOSWOC	Met Office Space Weather Operations Centre
MPV	Most Probable Value
NM	Neutron Monitor
NMDB	Neutron Monitor Data Base
NOAA	National Oceanic and Atmospheric Administration
PCA	Principal Component Analysis
PCR	Primary Cosmic Ray
PMT	Photo Multiplier Tube
RSS	Resonant Scattering Spectrometer
SCR	Solar Cosmics Ray
SEP	Solar Energetic Particle
SMMF	Solar Mean Magnetic Field
SSC	Storm Sudden Commencement
SSN	Sun-Spot Number
SWPC	Space Weather Prediction Center
WSO	Wilcox Solar Observatory

# 1 HiSPARC as a Space Weather Detector

## 1.1 Introduction

... [on daily variations (DV)] Dr. Rolf Butikofer (in a reply from Danislav Sapundzjiev, dasapund@meteo.be) said:

*"The daily cosmic ray variation near Earth is caused by the anisotropy of the cosmic ray intensity in the interplanetary space. Cosmic ray particles follow the field lines of the interplanetary magnetic field when they travel towards the interior of the heliosphere. Because of the rotation of the Earth, the angle between the asymptotic cone of acceptance of various energies at the location of ground-based cosmic ray detectors (neutron monitors) and the direction of the interplanetary magnetic field varies with a time period of 24 hours. As a consequence cosmic ray detectors look in different directions in the course of a day and observe therefore a diurnal variation. The daily variations of neutron monitors is mainly seen by high latitude stations which have asymptotic directions at low energies (rigidities) near the equator."*

### 1.1.1 HiSPARC Project

### 1.1.2 HiSPARC Detector

- design
  - scintillators
  - typical layouts (i.e. 2d or 4d)
  - trigger conditions

## 1.2 Aims

The HiSPARC project was set up with the detection philosophy of observing extended air showers (EAS), which are typically associated with PCRs with energy of  $\sim 10^{14}$  eV and above, that produce large footprints observable with many HiSPARC stations simultaneously. For PCRs with energy below  $\sim 10^{14}$  eV the air shower is small, with almost no observable footprint, and for PCRs with energy below  $\sim 10^{11}$  eV, there are typically less than one or two muons that reach the ground, making their observation difficult.

The HiSPARC detectors are capable of observing any muons that reach them, therefore the project was motivated by the existing network of muon detectors which may have the capability of observing the cosmic rays associated with space weather events.

The principle aim of the project was to determine whether the existing HiSPARC network is capable of observing space weather events. This was initially achieved by investigating the data during periods of space weather activity to search for the associated signatures. In addition, simulations of air showers initiated by CRs were conducted to understand the expected muon flux at ground level.

## 1.3 HiSPARC Properties

- Selected HS stations - Locations of stations - PLANETOCOSMICS simulations (explain) - Rigidities - Asymptotic viewing directions

To understand the PCR spectrum that the HiSPARC stations are capable of observing, PCR transport simulations were performed using the PLANETOCOSMICS software. PLANETOCOSMICS performs Geant4 Monte Carlo simulations of charged particle transport through Earth's magnetosphere based on Størmer's transport equation for charged particles (Desorgher et al., 2006). PLANETOCOSMICS simulates backward trajectories of charged particles from a given location (latitude,

longitude, and altitude) out to the magnetopause for a set of PCR rigidites.

For each trajectory there are two possible outcomes: (i) the particles trace out to the magnetopause where they escape Earth's magnetosphere, an allowed trajectory; (ii) the particles are sufficiently bent by the effect of the Earth's magnetosphere that they do not reach the magnetopause and cannot escape the Earth's magnetosphere, a forbidden trajectory (Desorgher et al., 2006). The coordinates of the asymptotic direction at the magnetosphere are provided as an output to the simulations projected back down to the Earth's surface. In this work PLANETOCOSMICS was configured with the Tsyganenko-89 model for the external magnetospheric magnetic field and the IGRF internal field model.

For each rigidity simulated, whether it was an allowed or forbidden trajectory was stored, which was used to provide an insight into the rigidity spectrum for a given station. From the allowed trajectories the effective cut-off rigidity ( $R_C$ ) for the stations was computed using equation (1.1), where  $R_U$  is the upper rigidity (the last allowed trajectory before the first forbidden trajectory);  $R_L$  is the lower rigidity (the last allowed trajectory before which all other trajectories with a lower rigidity are forbidden);  $\Delta R$  is the rigidity step size in the simulation (Desorgher et al., 2006; Herbst et al., 2013).

$$R_C = R_U - \sum_{i=R_L}^{R_U} \Delta R_i \quad (1.1)$$

The rigidity spectrum for each of the HiSPARC stations were investigated to determine  $R_C$  for each station. The cut-off rigidity calculated for the six HiSPARC stations for a vertical incidence upon the atmosphere (i.e.  $0^\circ$  zenith angle) are shown in Table 1.1 which show that there is little variation in  $R_C$  between the HiSPARC stations and that they observe protons with rigidities in excess of  $\sim 3$  GV. This analysis was initially carried out for the vertical direction (i.e. azimuth =  $0^\circ$ , zenith =  $0^\circ$ ); however further trajectories were simulated for different azimuth and zenith angles to determine the dependence of the rigidity spectrum on the

Table 1.1: Properties of some of the HiSPARC stations: geographic longitude ( $\lambda$ ), geographic latitude ( $\phi$ ), altitude ( $h$ ), and the geomagnetic vertical cut-off rigidity ( $R_C$ ) calculated from the PLANETOCOSMICS simulations.

Station Name/ID	$R_C$ [GV]	$\lambda$ [deg]	$\phi$ [deg]	$h$ [m]	No. Detectors
Nikhef/501	3.19	4.95 E	52.36 N	56.18	4
College Hageveld/203	3.18	4.63 E	52.35 N	53.71	2
Leiden/3001	3.23	4.45 E	52.17 N	54.08	2
Eindhoven/8001	3.44	5.49 E	51.45 N	70.12	2
Birmingham University/14001	3.06	1.93 W	52.45 N	204.14	4

detector acceptance angle. The analysis for the azimuthal dependence was carried out at a zenith angle of  $20^\circ$  as this is around the most probable angle for HiSPARC events, and the analysis of the zenith dependence was carried out at an azimuth angle of  $0^\circ$ .

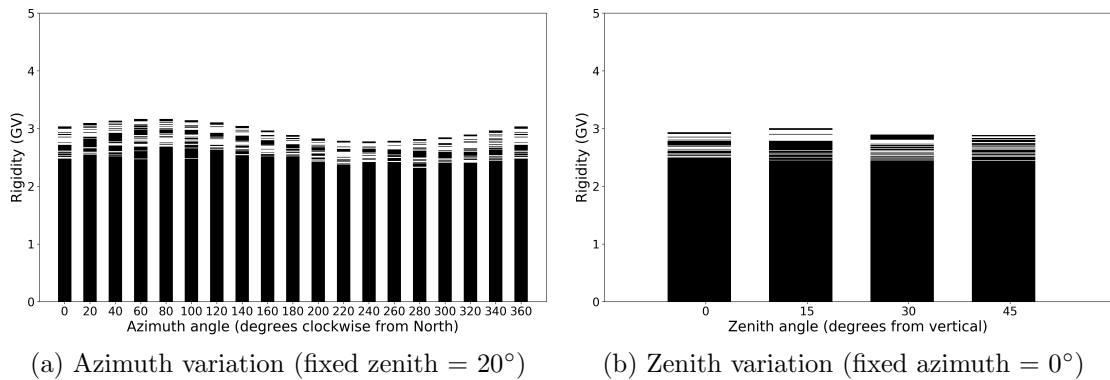


Figure 1.1: Azimuthal and zenith angle variations in the allowed and forbidden rigidity trajectories for HiSPARC station 501.

The small variation between HiSPARC stations is due to their close proximity in geographic latitude and longitude. The values of  $R_C$  calculated for the HiSPARC stations suggest that they should be able to observe higher energy SCRs, but may not be as susceptible as the higher latitude NMs where the effects of GLEs are highly observable.

As a results of the PLANETOCOSMICS simulations it is possible to understand the trajectories of particles that enter the Earth's magnetosphere prior to arrival at the muon detector.

Figure 1.2...

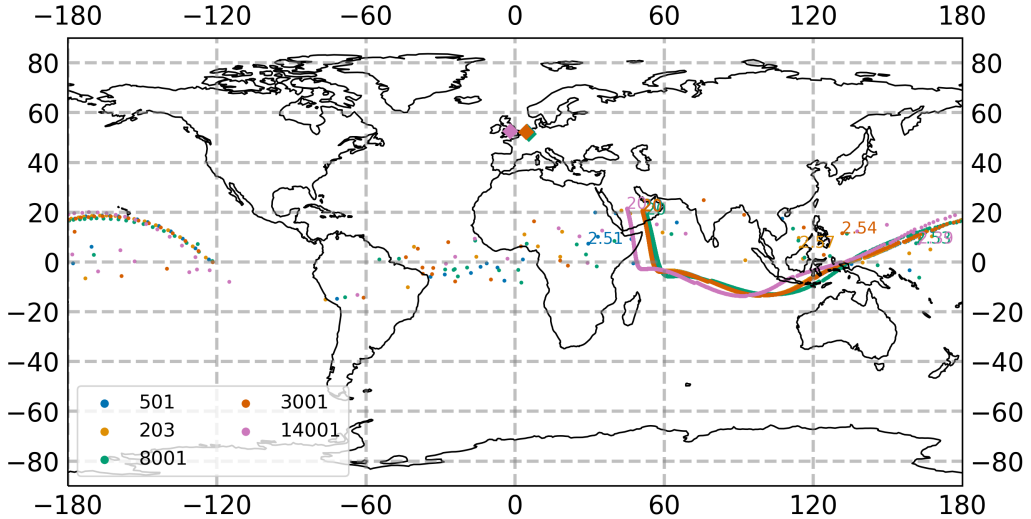


Figure 1.2: The vertical asymptotic viewing directions of 5 HiSPARC stations. The rigidity range of the simulations were from  $1.0 \text{ GV} < R < 20.0 \text{ GV}$ , and the results are plotted in geographic coordinates on January 20th 2005. The diamonds correspond to the HS ground location and the circles correspond to the AVD for a specific rigidity value.

## 1.4 HiSPARC Observations

[discuss preliminary observation of space weather FDs and GLEs for the events and singles data...]

[end with discussion on unknown PCRs observable and the effect of atmospheric weather conditions that need to be accounted for]

The effects of space weather on CRs has been outlined in [REF intro]. It was highlighted during communication with the UK Met Office that observations of GLEs are of more interest and importance to space weather forecasts and nowcasts. FDs are of lower interest and importance, however they were still searched for within the HiSPARC data. The events that were looked for within the HiSPARC data are outlined in Table 1.2.

### 1.4.1 HiSPARC Observations of Ground Level Enhancements

Initial searches for evidence of GLEs within the HiSPARC data were conducted for GLE 70, 71, and 72, as they are the only GLEs that span the operational epoch of

Table 1.2: Space weather events investigated within the HiSPARC data. The percentage change column provides a reference of how much the CR counts observed by the NM station at Oulu ( $R_c=0.81$  GV) increased or decreased by, due to the space weather event.

GLE Onset	GLE	% Change (Oulu)	FD Onset	% Change (Oulu)
13/12/2006	70	~ 100%	08/03/2012	~ 5%
17/05/2012	71	~ 15%	14/07/2012	~ 3%
10/09/2017	72	~ 5%	21/12/2014	~ 5%
			06/09/2017	~ 2%
			07/09/2017	~ 8%

the HiSPARC network.

Figure 1.3...

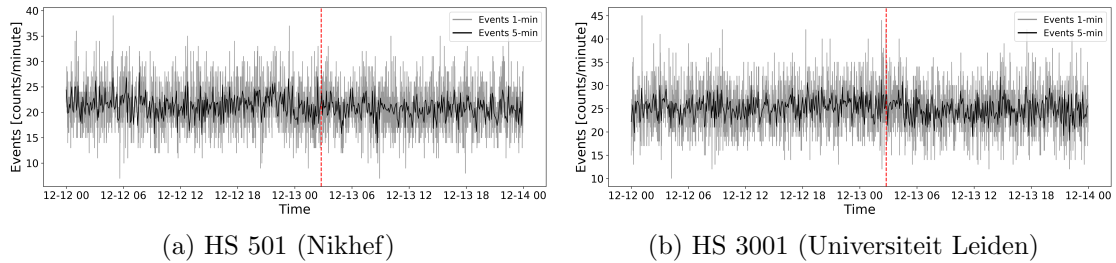


Figure 1.3: HiSPARC data for stations 501 and 3001 around the epoch of GLE 70. The plot shows the minute-averaged and 5-minute-averaged trigger events between detectors within the station. The vertical red, dashed line depicts the approximate onset time of the GLE.

Figure 1.4...

Figure 1.5...

... no clear GLE seen...

#### 1.4.2 HiSPARC Observations of Forbush Decreases

Figure 1.6...

Figure 1.7...

Figure 1.8...

Figure 1.9...

... no clear FDs seen...

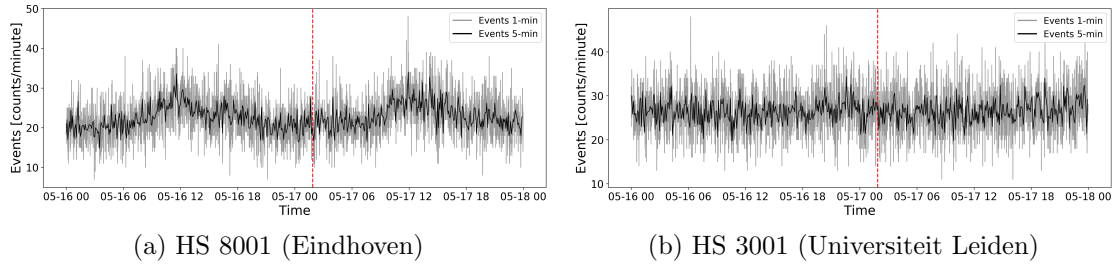


Figure 1.4: HiSPARC data for stations 8001 and 3001 around the epoch of GLE 71. The plot shows the minute-averaged and 5-minute-averaged trigger events between detectors within the station. The vertical red, dashed line depicts the approximate onset time of the GLE.

## 1.5 Air Shower Simulations

In order to understand the footprint of air showers produced by PCRs, simulations of air showers were performed for a range of primary proton and  $\alpha$ -particle energies.

To simulate the CR air shower development, we employ CORSIKA (**C**Osmic **R**ay **S**Imulations for **K**Ascade), a Monte Carlo programme providing detailed simulations of the evolution of air showers initiated by cosmic rays particles through the atmosphere (Heck & Pierog, 2017). The particles in the CORSIKA simulations are tracked through the atmosphere until they undergo interactions with atmospheric nuclei, decay due to their instability, or reach the ground level defined as the end of the simulation.

Proton and  $\alpha$ -particle initiated air showers were generated with energies ranging from  $10^9$  to  $10^{20}$  eV, and  $4 \times 10^9$  to  $10^{20}$  eV, respectively. In total  $\sim 230000$  proton-initiated showers were simulated and  $\sim 180000$   $\alpha$ -particle-initiated air showers were simulated. The list of simulated air shower PCRs is shown in Table 1.3. For high energy, inelastic hadronic interactions within CORSIKA the QGSJET-II [REF] model was selected. Interactions of hadrons with energies below 80 GeV are simulated using GHEISHA [REF], which allowed for the simulation of PCRs in the regime of SCRs. In addition to these hadronic interactions, electromagnetic interactions within the CORSIKA simulations were described by the EGS4 [REF] model.

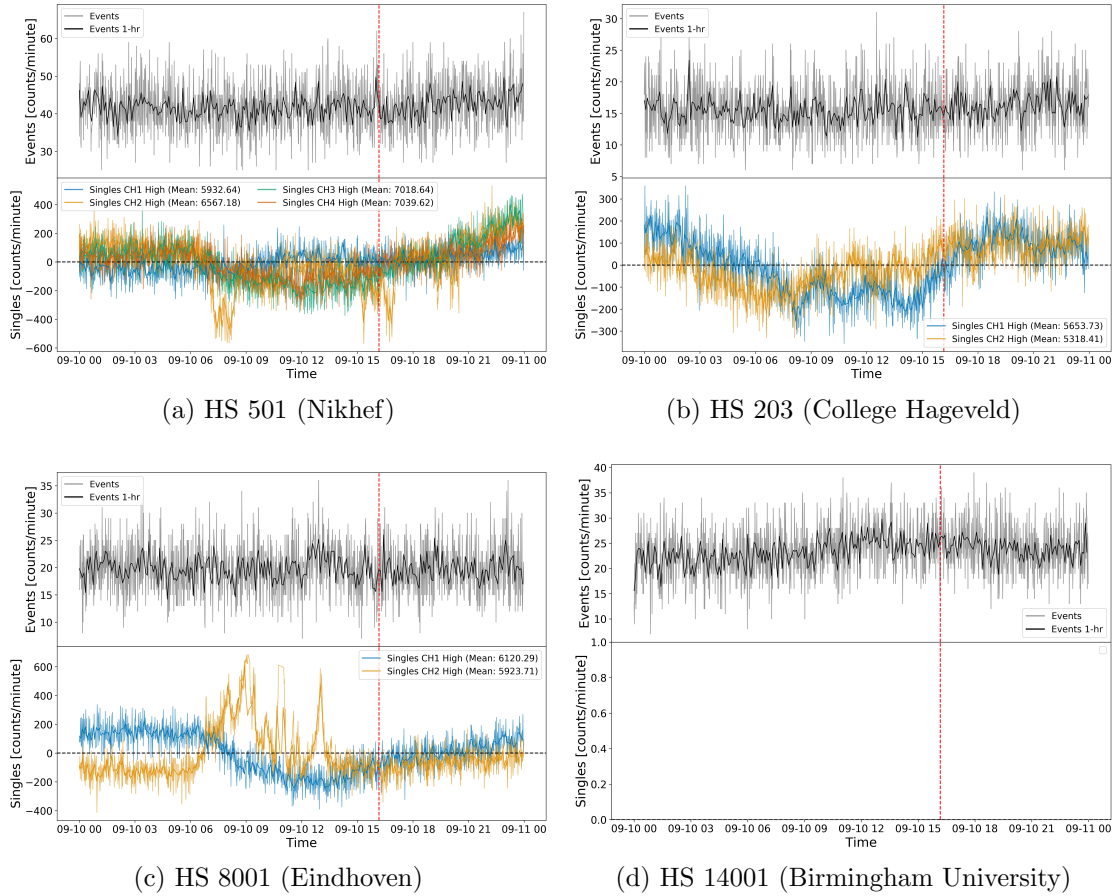


Figure 1.5: HiSPARC data for 4 stations around the epoch of GLE 72. The top panel of each subplot shows the minute-averaged trigger events between detectors within the station, while the bottom panel shows the mean-shifted, minute-averaged counts by each individual detector in the station. The vertical red, dashed line depicts the approximate onset time of the GLE.

Furthermore CORSIKA has a minimum muon energy limit that can be simulated of 10 MeV.

There are several other user-definable setting within CORSIKA which are explained in-depth in the CORSIKA user's guide (Heck & Pierog, 2017). The settings chosen within these simulation are briefly discussed below. Simulation thinning was enable in CORSIKA to reduce computation time and reduce the output file size. The observation level at which point the simulation cease was set at 100 m above sea level (compared to the  $\sim 50$  m typical of the stations, however this difference is negligible for the air shower development.) The pre-defined central European atmosphere in October was used for all simulations, and western-European magnetic

Table 1.3: PCRs simulated using CORSIKA.

Protons				$\alpha$ -Particles			
E <sub>PCR</sub> (eV)	N <sub>sims</sub>						
1.00E+09	10000	2.98E+12	1000	4.00E+09	10000	1.00E+13	1000
1.27E+09	10000	3.79E+12	1000	4.28E+09	10000	1.78E+13	100
1.62E+09	10000	4.83E+12	1000	5.46E+09	10000	3.16E+13	100
2.07E+09	10000	6.16E+12	1000	6.95E+09	10000	5.62E+13	100
2.64E+09	10000	7.85E+12	1000	8.86E+09	10000	1.00E+14	100
3.36E+09	10000	1.00E+13	1000	1.00E+10	10000	1.78E+14	50
4.28E+09	10000	1.78E+13	100	1.13E+10	10000	3.16E+14	50
5.46E+09	10000	3.16E+13	100	1.44E+10	10000	5.62E+14	50
6.95E+09	10000	5.62E+13	100	1.83E+10	10000	1.00E+15	10
8.86E+09	10000	1.00E+14	100	2.34E+10	10000	1.78E+15	10
1.00E+10	10000	1.78E+14	50	2.98E+10	10000	3.16E+15	10
1.13E+10	10000	3.16E+14	50	3.79E+10	10000	5.62E+15	10
1.44E+10	10000	5.62E+14	50	4.83E+10	10000	1.00E+16	10
1.83E+10	10000	1.00E+15	10	6.16E+10	10000	1.78E+16	10
2.34E+10	10000	1.78E+15	10	7.85E+10	10000	3.16E+16	10
2.98E+10	10000	3.16E+15	10	1.00E+11	10000	5.62E+16	10
3.79E+10	10000	5.62E+15	10	1.27E+11	1000	1.00E+17	10
4.83E+10	10000	1.00E+16	10	1.62E+11	1000	1.78E+17	10
6.16E+10	10000	1.78E+16	10	2.07E+11	1000	3.16E+17	10
7.85E+10	10000	3.16E+16	10	2.64E+11	1000	5.62E+17	10
1.00E+11	10000	5.62E+16	10	3.36E+11	1000	1.00E+18	10
1.27E+11	1000	1.00E+17	10	4.28E+11	1000	1.78E+18	10
1.62E+11	1000	1.78E+17	10	5.46E+11	1000	3.16E+18	10
2.07E+11	1000	3.16E+17	10	6.95E+11	1000	5.62E+18	10
2.64E+11	1000	5.62E+17	10	8.86E+11	1000	1.00E+19	10
3.36E+11	1000	1.00E+18	10	1.13E+12	1000	1.78E+19	10
4.28E+11	1000	1.78E+18	10	1.44E+12	1000	3.16E+19	10
5.46E+11	1000	3.16E+18	10	1.83E+12	1000	5.62E+19	10
6.95E+11	1000	5.62E+18	10	2.34E+12	1000	1.00E+20	10
8.86E+11	1000	1.00E+19	10	2.98E+12	1000		
1.13E+12	1000	1.78E+19	10	3.79E+12	1000		
1.44E+12	1000	3.16E+19	10	4.83E+12	1000		
1.83E+12	1000	5.62E+19	10	6.16E+12	1000		
2.34E+12	1000	1.00E+20	10	7.85E+12	1000		

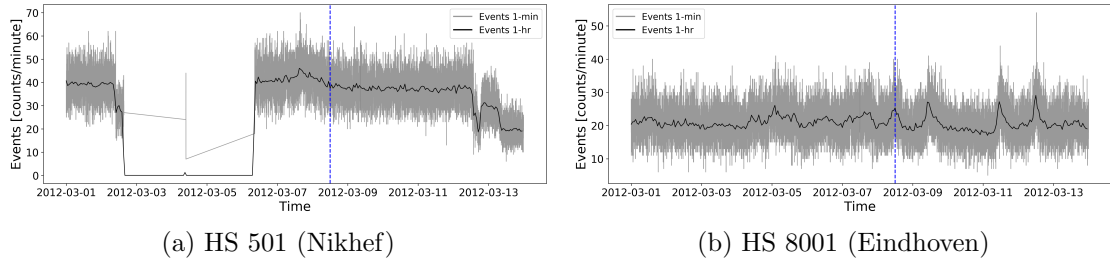


Figure 1.6: HiSPARC data for stations 501 and 8001 around the epoch of the FD in March 2012. The plot shows the minute-averaged and hourly-averaged trigger events between detectors within the station. The vertical blue-dashed line shows the approximate onset-time of the FD.

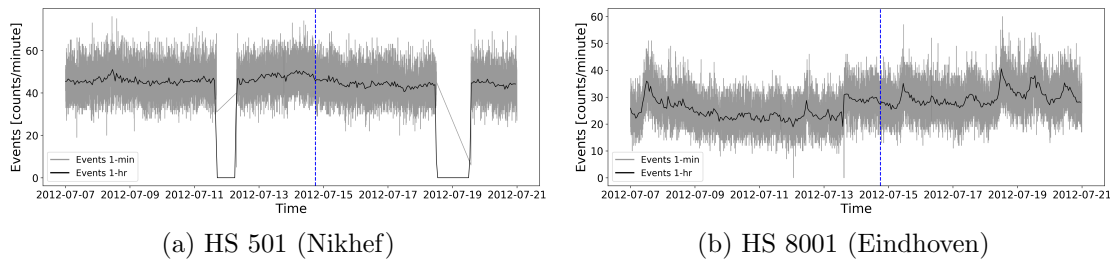


Figure 1.7: HiSPARC data for stations 501 and 8001 around the epoch of the FD in July 2012. The plot shows the minute-averaged and hourly-averaged trigger events between detectors within the station. The vertical blue-dashed line shows the approximate onset-time of the FD.

field was used as calculated with the *Geomag* programme [REF]:  $B_x = 18.799 \mu\text{T}$  and  $B_z = 44.980 \mu\text{T}$ .

### 1.5.1 Air Shower Footprints

The average footprint of muons at ground level was acquired from the output CORSIKA simulations. This was achieved by simply taking the distribution of the muons at ground level at the end of the simulation as a function of their distance from the shower core for each individual simulation realisation. For a given PCR energy the average air shower footprint distribution is calculated by combining the individual simulation realisations.

The interpretation of Figure 1.10 can provide an understanding of the minimum energy of PCRs observable by the different stations within the HiSPARC network. The typical separation between the detectors in a HiSPARC station is  $\sim 10 \text{ m}$ ,

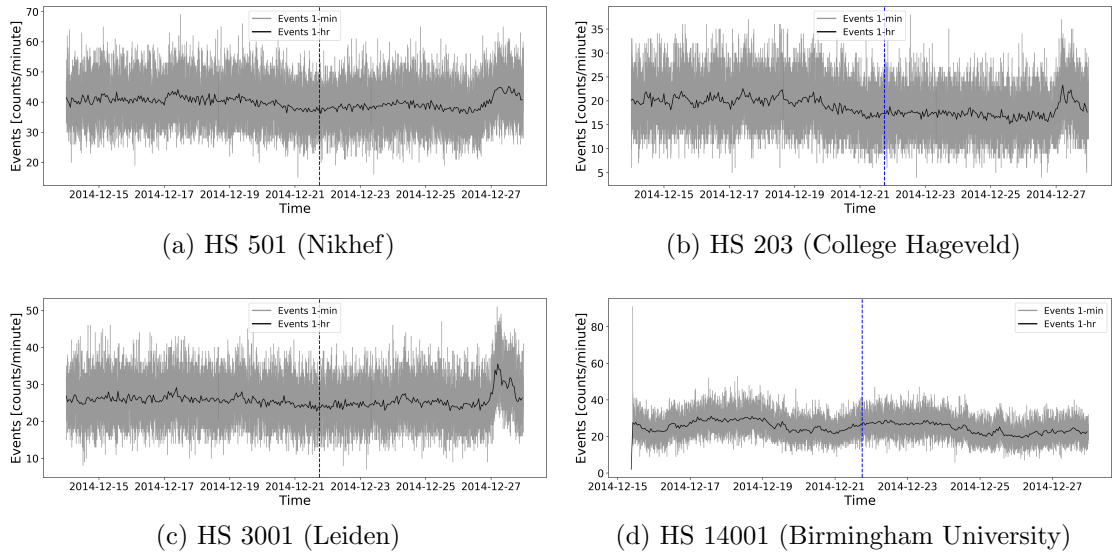


Figure 1.8: HiSPARC data for 4 stations around the epoch of the FD in December 2014. The plot shows the minute-averaged and hourly-averaged trigger events between detectors within the station. The vertical blue-dashed line shows the approximate onset-time of the FD.

however the separation between detectors can be up to as much as 20 m or as low as a couple of metres. This analysis of the air shower footprint shows the variation in PCR energy sampled varies marginally over this range of distances and suggests that HiSPARC stations will typically observe PCR with an energy of  $\sim 10^{14} - 10^{15}$  eV to meet the required trigger conditions.

### 1.5.2 Muon Flux

From the air shower simulations it is possible to gain an estimate of the muon flux at ground-level based on the number of

## 1.6 Standardisation of HiSPARC Data

### 1.6.1 Motivation

- HiSPARC stations are individually managed and guidelines aren't stringent - Variability between stations exists and also apparently between detectors within a station (i.e. see singles during GLE 72)

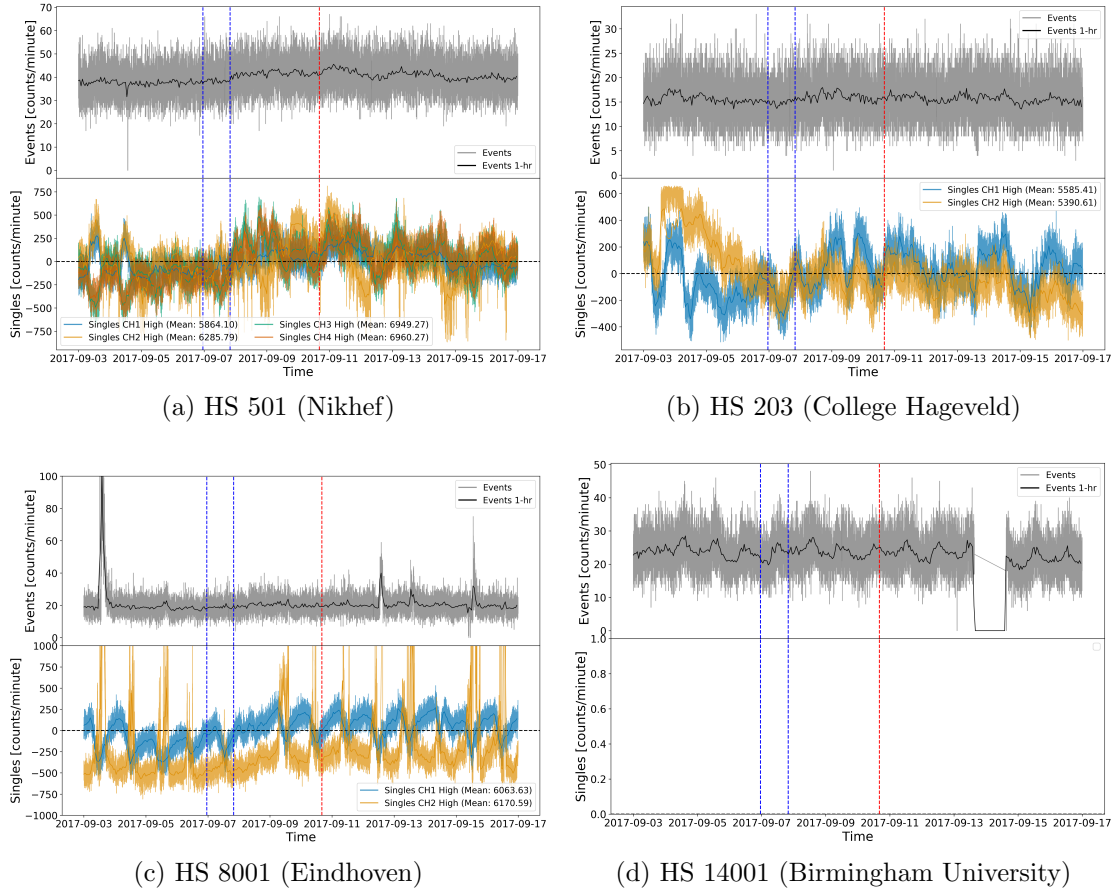


Figure 1.9: HiSPARC data for [n] stations around the epoch in which there were several FDs close to the onset of GLE 72. The top panel of each subplot shows the minute-averaged trigger events between detectors within the station, while the bottom panel shows the mean-shifted, minute-averaged counts by each individual detector in the station. The vertical blue-dashed lines show the approximate onset-times of the two FDs observed around this epoch and the red-dashed line depicts the approximate onset time of the GLE.

### 1.6.2 Barometric Correction

It is understood that observations made by ground-based CR detectors are susceptible to atmospheric conditions. Atmospheric pressure effects the CR travel path due to the expansion and contraction of the atmosphere with varying pressure; hence the CR counts are observed to be negatively correlated to atmospheric pressure as shown for both NMs and MDs in Figure 1.12. A correction for this barometric effect is routinely applied as part of the data calibration for all NM stations within the NMDB NEST, but there is no such process in the HiSPARC network.

The method of correcting for the barometric effect is discussed widely in the

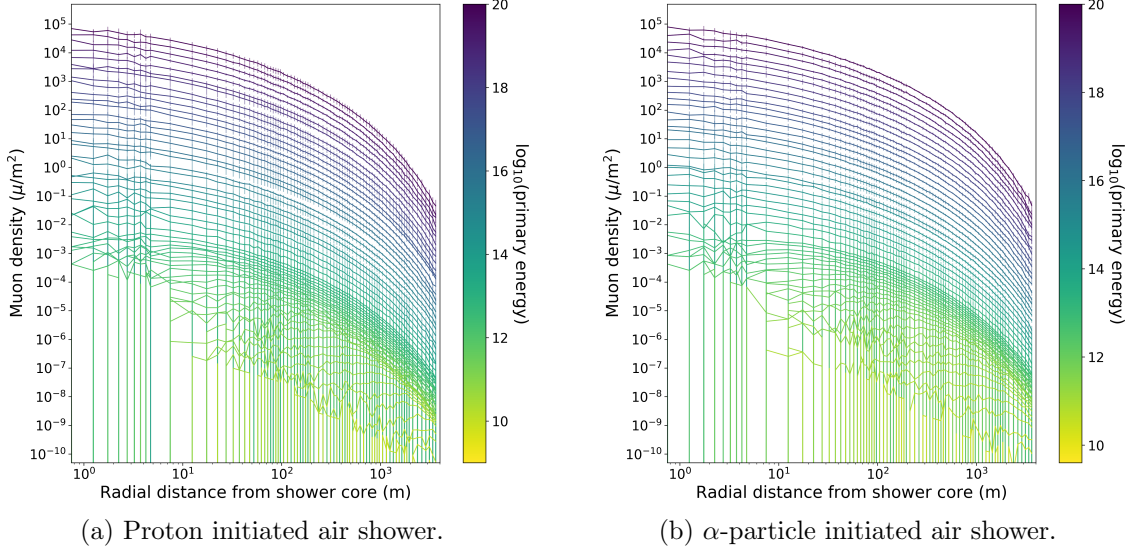


Figure 1.10: Mean muon density footprints for (a) proton-initiated air showers and (b)  $\alpha$ -particle-initiated air showers with intial PCR trajectories with zenith angles  $\theta = 0^\circ$  and various PCR energies. The error bars given represent  $1\sigma$ .

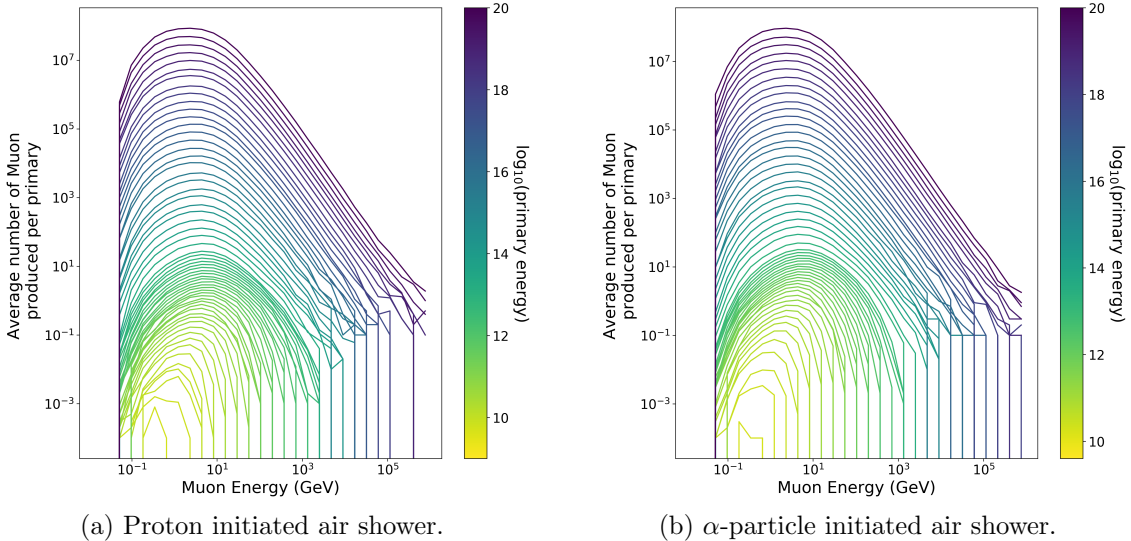


Figure 1.11: Mean number of muons produced at ground level by the PCR for (a) proton-initiated air showers and (b)  $\alpha$ -particle-initiated air showers, for various PCR energy. The uncertainty bars given represent  $1\sigma$ .

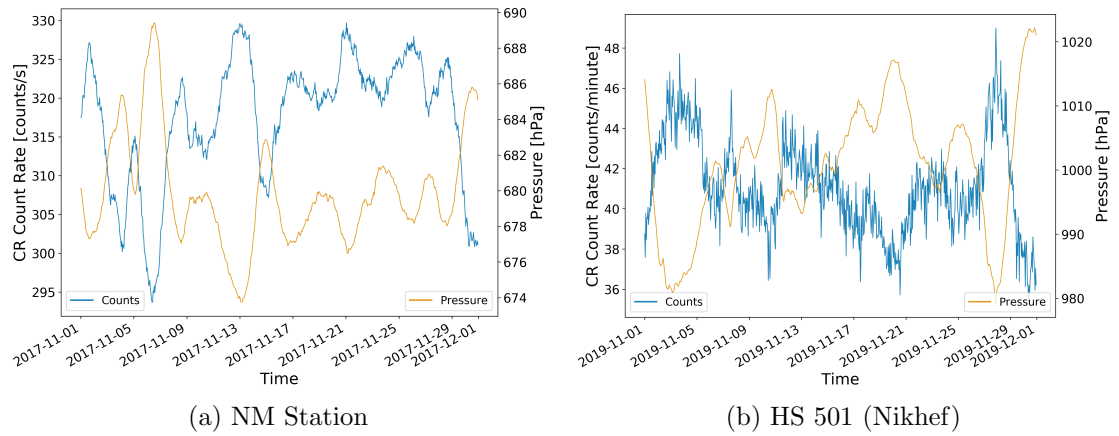


Figure 1.12: ...

literature regarding NMIs and is shown to depend on the barometric coefficient. Assuming the cosmic ray flux variation, absent of the atmospheric effects, is reasonably stable, then a simple correction can be made. The CR variations ( $N$ ) that depend on the local atmospheric pressure are described by equation (1.2), where  $\Delta N$  is the change in count rate,  $\beta$  is the barometric coefficient, and  $\Delta P = P - P_0$  is the deviation in pressure from the average ( $P_0$ ) in the given time-period (Paschalis et al., 2013):

$$\Delta N = -\beta N \Delta P \quad (1.2)$$

Through the integration of equation (1.2), the solution shows the dependence of cosmic ray intensity on pressure as given in equation (1.3).

$$N = N_0 e^{-\beta \Delta P} \quad (1.3)$$

Therefore by taking the logarithm of equation (1.3), one can obtain the barometric coefficient by fitting the straight line given by equation (1.4) to the observed data, where  $N_0$  may be assumed as the mean count rate over the given time-period of observations considered.

$$\ln\left(\frac{N}{N_0}\right) = -\beta \Delta P \quad (1.4)$$

A demonstration of the barometric correction method of fitting a straight line to the data described by equation (1.4) is shown for both a NM and a HiSPARC station in Figure 1.13.

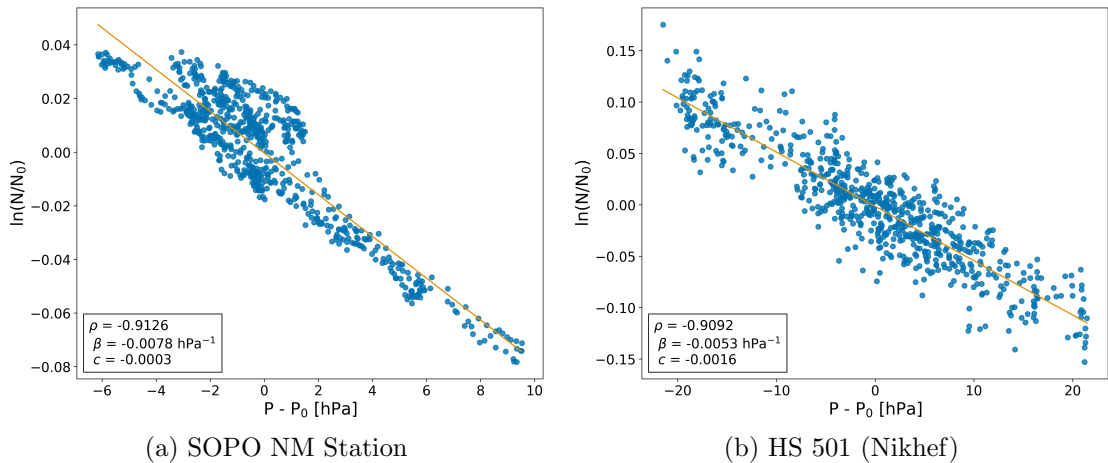


Figure 1.13: The barometric coefficient calculation: (a) during November 2017 for the South Pole (SOPO) NM station, (b) during November 2019 for HiSPARC station 501 at Nikhef.

An online barometric coefficient tool is available which allows user to perform the barometric correction for a given station over a user-defined epoch (<http://cosray.phys.uoa.gr/index.php/data/nm-barometric-coefficient>). Using this tool, it was possible to provide a comparison between the method used in this work to that of the online NM barometric correction tool which is used for the correction of the NMDB stations. This is provided in Figure 1.14 for monthly corrections throughout 2017 for the NM station at the South Pole (SOPO).

Figure 1.14 shows a close agreement between the barometric coefficient calculated in this work and those acquired from the online tool for the SOPO NM. This was also true for other stations tested (APTY and ROME), thus providing confidence that the method used in this work was suitable for application on the HiSPARC data. The barometric correction was performed on the stations where sufficient

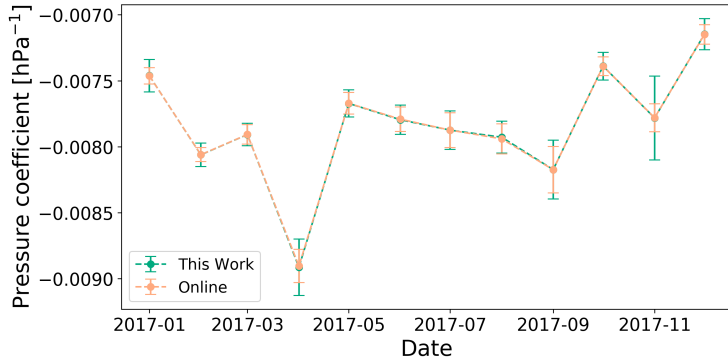


Figure 1.14: A comparison between the monthly barometric coefficient computed in this work and using the online barometric coefficient tool throughout the year 2017 for the SOPO NM station.

pressure data and count rates exist, and were re-investigated to determine whether the space weather events were observed in the HiSPARC data. These results are provided in Section 1.7.

### 1.6.3 Temperature Correction

It has been discussed in the literature that the effect of atmospheric temperature on muon intensity has to be treated differently to the pressure effect (Berkova et al., 2011), as the temperature influences both the creation and disintegration processes for muons, such that there is a positive effect and a negative effect on muon intensity as a consequence of temperature variations (Mendonça et al., 2016).

The positive effect is related to pion decay and its dependence on temperature variation. The higher the temperature, the lower the atmospheric pion absorption, which implies a higher generation rate of muons (Mendonça et al., 2016).

The negative effect corresponds to the decrease of muon intensity at ground level as the muon average path length varies with temperature. Due to the heating and the expansion of the atmosphere during summer periods muons are produced higher in the atmosphere; hence the muon propagation path increases meaning more atmosphere for muons to traverse before reaching the ground, and an increased decay probability and ionisation losses (Savi et al., 2015; Mendonça et al., 2016).

Due to the difference in decay probability, the negative effects dominate for low

energy muons (i.e. those detected by ground-level MDs), and the positive effect dominates for high energy muons (i.e. those detected by underground MDs) (Berkova et al., 2011); therefore it is expected that the negative effect should dominate for the HiSPARC network. Temperature effects are also observed by NMs; however the effect is less significant than for MDs hence temperature corrections are not widely applied for NMs (Mendon{\c{c}}a et al., 2016).

This is in contradiction with the observations of diurnal variation with the HiSPARC detector, as one can quite clearly see that the HiSPARC stations register higher count rates during local noon.

Several methods of correcting for the negative temperature effect are summarised by Berkova et al. (2011) which utilise different measures of atmospheric temperature when performing the temperature correction. Mendon{\c{c}}a et al. (2016) provides a comparative summary of these methods applied to correct for atmospheric temperature variations observed by GMDN detectors. The methods discussed here however are typically applied over long timescales of years with low temporal resolution rather than to account for short timescale variations with periods of less than a day; hence the suitability of these methods is uncertain.

Mendon{\c{c}}a et al. (2016) concludes that correcting for temperature using the atmospheric mass weighted temperature is one of the most suitable methods for the GMDN as it allows for the highest correlation between long-term CR variations and temperature. The mass weighted method is an approximation for integrating over the vertical atmospheric temperature as is given in Eq. (1.5):

$$\left( \frac{\Delta N}{N} \right)_T = \bar{\alpha} \int_0^{h_0} \delta T(h) dh = \sum_{i=0}^n \frac{x(h_i) - x(h_{i+1})}{x(h_0)} T(h_i) = \alpha_{\text{MSS}} \delta T_{\text{MSS}} \quad (1.5)$$

where  $h_0$  is the closest to ground altitude;  $\delta T_{\text{MSS}}$  is the deviation of the mass weighted atmospheric temperature;  $T(h_i)$  is the temperature in degrees kelvin ob-

served at the altitude  $h_i$ ;  $x(h_i)$  is the atmospheric depth at the altitude  $h_i$  which is given by Eq. 1.6:

$$x(h) = \int_h^\infty \rho(h) dh \rho(h) = \frac{P(h)}{T(h)} \frac{M_{mol}}{R} \quad (1.6)$$

where  $P(h)$  is the atmospheric pressure profile as a function of depth;  $T(h)$  is the atmospheric temperature;  $\rho(h)$  is the air density at a given altitude  $h$ ;  $M_{mol}$  is the molar mass of air;  $R$  is the universal gas constant.

The temperature correction is therefore used in a formalism the same as Eq. (1.4), replacing replacing  $\beta$  for  $\alpha$  and  $\Delta P$  for  $\Delta T$ .

In addition it is discussed by Berkova et al. (2011) and Mendon{\c{c}}a et al. (2016) that the effective generation level temperature is a suitable assumption for this purpose. This method is based on the assumption that muons are mostly generated at a certain isobaric level, taken as 100 mbar, and therefore the temperature at 100 mbar in the atmospheric pressure profile is used,  $T_{100\text{mbar}}$ .

As discussed above, Mendon{\c{c}}a et al. (2016) provide this as a method for correcting for the long-term variation in atmospheric temperature which varies seasonally rather than to correct for diurnal variations; therefore it is unsure how relevant this method of atmospheric temperature correction will be to the diurnal variations observed in the HiSPARC data.

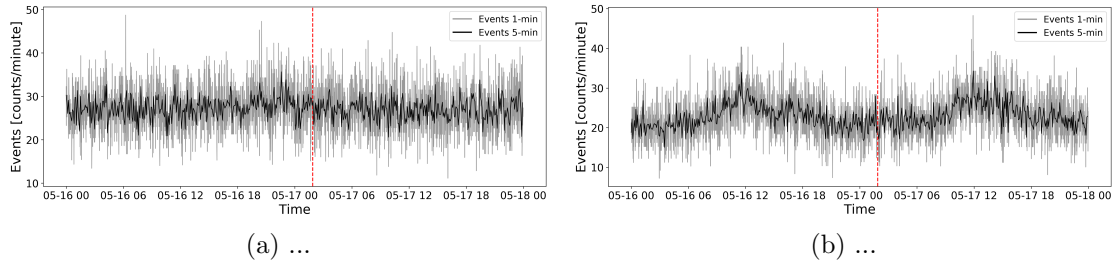


Figure 1.15: Pressure corrected HiSPARC data for 2 stations around the epoch of GLE 71. The top panel of each subplot shows the minute-averaged trigger events between detectors within the station, while the bottom panel shows the mean-shifted, minute-averaged counts by each individual detector in the station. The vertical red, dashed line depicts the approximate onset time of the GLE.

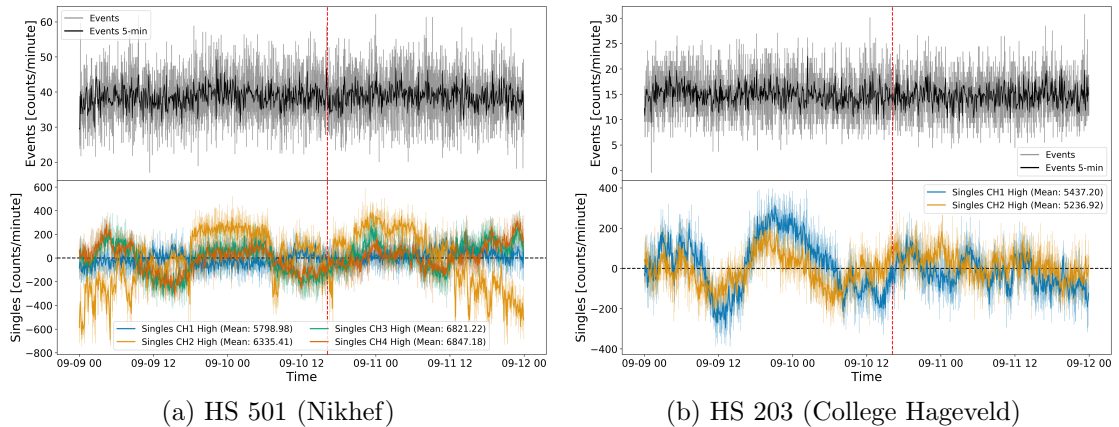


Figure 1.16: Pressure corrected HiSPARC data for 2 stations around the epoch of GLE 72. The top panel of each subplot shows the minute-averaged trigger events between detectors within the station, while the bottom panel shows the mean-shifted, minute-averaged counts by each individual detector in the station. The vertical red, dashed line depicts the approximate onset time of the GLE.

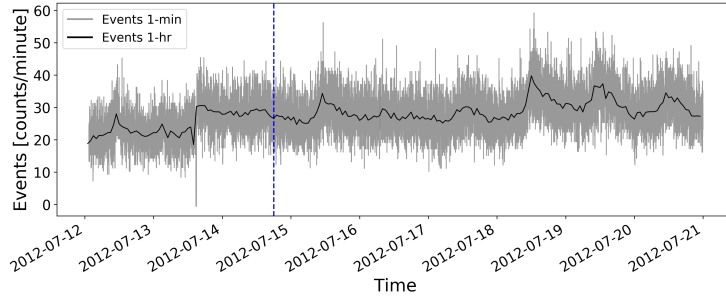


Figure 1.17: ...

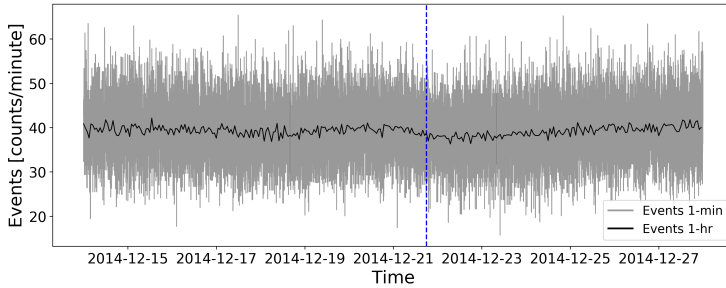


Figure 1.18: ...

## 1.7 HiSPARC Observations After Pressure Corrections

### 1.7.1 Pressure Corrected Observations of Ground Level Enhancements

### 1.7.2 Pressure Corrected Observations of Forbush Decreases

## 1.8 Discussion

Throughout this chapter the feasibility of using the HiSPARC network of muon detectors has been analysed. This has involved performing cosmic ray air shower simulations using CORSIKA and performing backwards

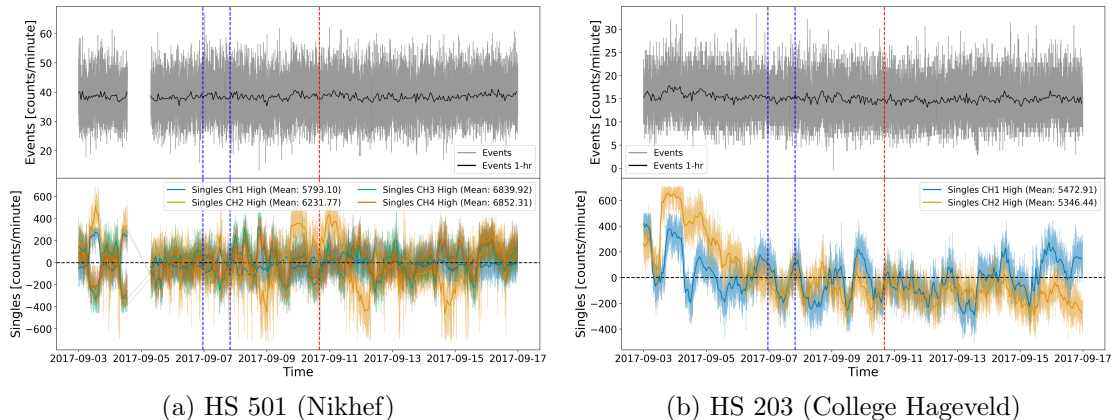


Figure 1.19: Pressure corrected HiSPARC data for [n] stations around the epoch in which there were several FDs close to the onset of GLE 72. The top panel of each subplot shows the minute-averaged trigger events between detectors within the station, while the bottom panel shows the mean-shifted, minute-averaged counts by each individual detector in the station. The vertical blue-dashed lines show the approximate onset-times of the two FDs observed around this epoch and the red-dashed line depicts the approximate onset time of the GLE.

## 2 Galactic Cosmic Ray Behaviour During Solar Cycle 24

*The majority of the text in this chapter is taken from Ross & Chaplin (2019). I was first author on this journal article and conducted the work of the investigation. Section [CITE] has been written since the publication of Ross & Chaplin (2019) to document the continuation of this analysis to the end of Solar Cycle 24.*

### 2.1 Introduction

Galactic cosmic rays (GCRs) are charged particles and atomic nuclei with energies spanning the range from a few MeV up to approximately  $10^{21}$  eV, that encroach upon the Earth from all directions (Giacalone, 2010). They mainly originate outside the solar system, within the Milky Way; however they are also expected to originate from other galaxies (Aab et al., 2017). GCRs at the top of the atmosphere are mostly composed of protons ( $\sim 87\%$ ) and  $\alpha$ -particles ( $\sim 12\%$ ), with a smaller contribution ( $\sim 1\%$ ) from heavier nuclei (Dunai, 2010).

When cosmic rays (CRs) enter the atmosphere, they interact with atmospheric atoms and produce cascades of secondary particles, which at ground level are primarily neutrons and muons. Neutron monitors (NMs) and muon detectors (MDs) located at different locations on Earth have been used since the 1950s to observe GCRs. Information on GCRs prior to the modern epoch of NMs and MDs, and the space age, rely on the studies of cosmogenic isotope records from ice cores and tree

rings (Owens & Forsyth, 2013).

It has long been established that there exists an anti-correlation between GCR intensity and the level of solar activity, over a cyclic 11-year period, with perhaps some time-lag (Forbush, 1958; Parker, 1965; Usoskin et al., 1998; Van Allen, 2000). Figure 2.1 shows clearly the anti-correlation between GCRs and sunspot number (SSN).

It is well known that the 11-year solar activity cycle is in fact a 22-year cycle - the Hale cycle - which describes the alternating polarity of the large-scale solar magnetic field (Thomas et al., 2014a). The interchanging peaked and flat-topped shape of GCR intensity in Figure 2.1 is a manifestation of this effect in addition to other CR transport processes (Aslam & Badruddin, 2012).

The polarity of the solar field,  $A$ , is taken to be negative when the field axis is aligned with the axis of rotation, and positive when the opposite is true (Thomas et al., 2014a). The solar field polarity conventionally is described in combination with particle charge,  $q$ , due to the effect of curvature and gradient drift on charged particles; thus it is customary to define the solar polarity as  $qA$ . Vertical lines showing the approximate epochs at which the polarity reverses are plotted in Figure 2.1 (Janardhan et al., 2018; Thomas et al., 2014a).

Particle drifts differ during different  $qA$  cycles, with positive CRs (i.e. protons) predominantly arriving into the heliosphere from the heliospheric poles and outwards to Earth during periods when  $qA > 0$ , whereas when  $qA < 0$ , positive CRs predominantly arrive at Earth inwards along the heliospheric current sheet (HCS) (Belov, 2000; Thomas et al., 2014b). As the solar magnetic dipole axis is tilted to the solar rotation axis, so is the HCS; the HCS tilt varies with solar cycle and is typically smaller during solar minimum and larger during solar maximum (Owens & Forsyth, 2013). The tilt angle of the HCS has also been shown to be strongly correlated to the GCR intensity and the GCR lag behind the solar activity (Belov, 2000; Mavromichalaki et al., 2007).

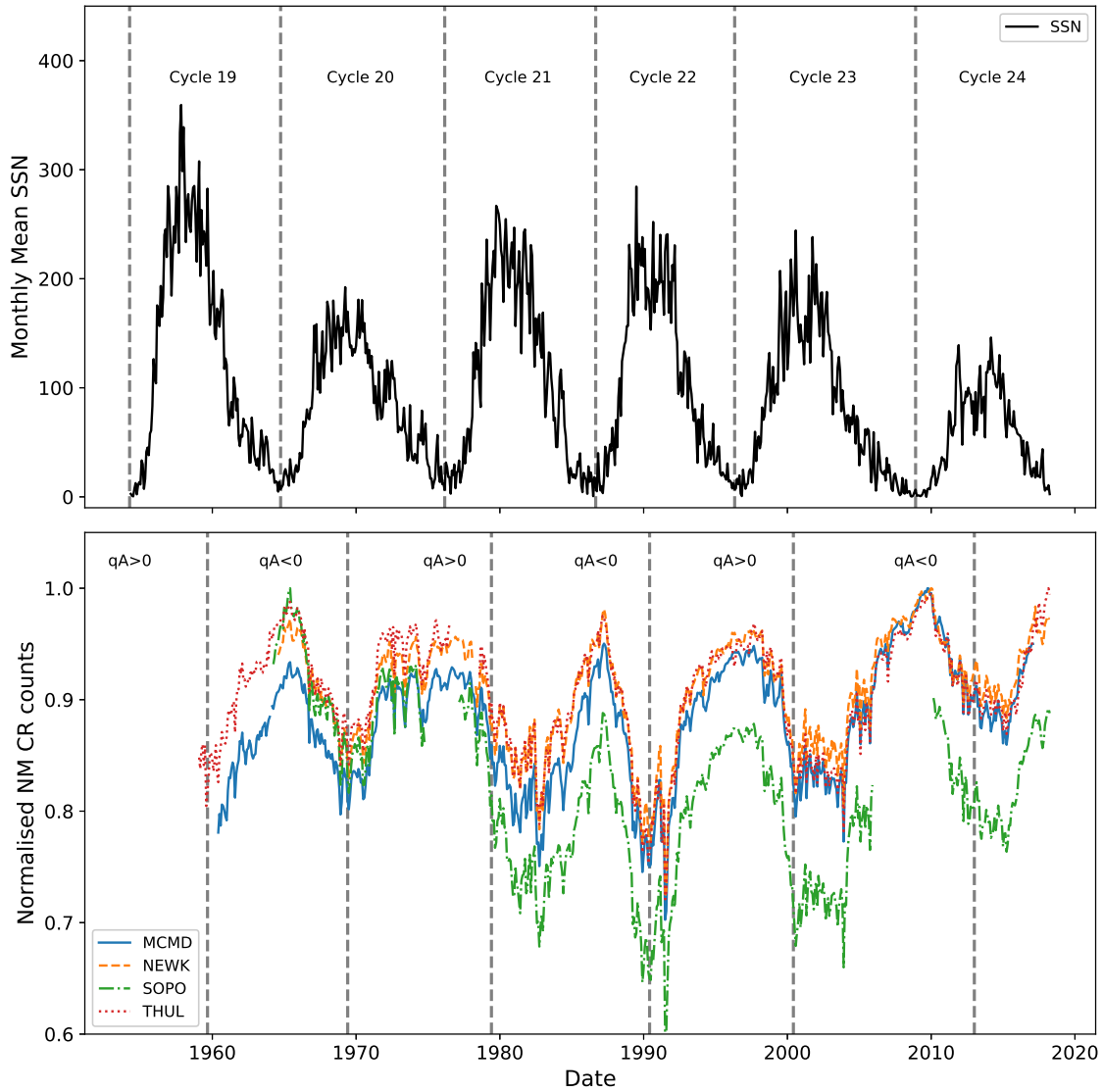


Figure 2.1: SSN (top), with vertical lines showing the beginning of each solar cycle. Cosmic ray intensity recorded by NM (bottom), with vertical lines showing the approximate epochs of solar magnetic field polarity reversals. (MCMD = McMurdo, NEWK = Newark, SOPO = South Pole, THUL = Thule).

Aslam & Badruddin (2012, 2015) found that the different processes of CR transport have varying levels of importance throughout the solar activity cycle, but around solar maximum it is likely that drifts play less of a role and disturbances in the solar wind (and hence HCS) are the predominant factor of CR modulation. Even cycles encounter  $qA < 0$  polarity during their onset phase and  $qA > 0$  during their declining phase, thus experiencing a faster GCR recovery after solar maximum as the GCRs predominantly enter the heliosphere from the heliospheric poles and experience an outwards drift towards Earth. Odd cycles encounter  $qA > 0$  polarity during their onset phase and  $qA < 0$  during their declining phase and so experience a slower recovery after solar maximum, as the GCRs predominantly enter the heliosphere along the HCS. When the HCS is tilted and disturbed during the declining activity phase, the path length that GCRs must travel to Earth increases; hence resulting in an increased time-lag.

Several studies have demonstrated the lag between GCR and solar activity proxies is approximately zero (i.e. no lag) during even solar cycles, and that there exists a lag of around a year or more during odd solar cycles (Usoskin et al., 1998; Mavromichalaki et al., 2007; Singh et al., 2008).

Van Allen (2000) showed through cross-plotting the annual mean intensity of GCRs against sunspot number (SSN) between 1953 and 1999 (covering solar cycles 19-22), that there is a distinct difference in the plot shapes between the different solar cycles, with 19 and 21 producing broad ovals, and 20 and 22 as approximately flat lines. The striking difference between odd-numbered and even-numbered cycles is shown for cycles 19-24 in Figure 2.2. It is believed that this hysteresis effect is caused by the combination of the heliospheric magnetic field (HMF), solar magnetic field polarity and thus the particle drift, and the tilt of the HCS leading to a slow recovery of GCR intensity after maxima in odd cycles and a fast recovery after maxima in even cycles (Van Allen, 2000; Belov, 2000; Thomas et al., 2014a).

An extension of this work has since been carried out by Inceoglu et al. (2014)

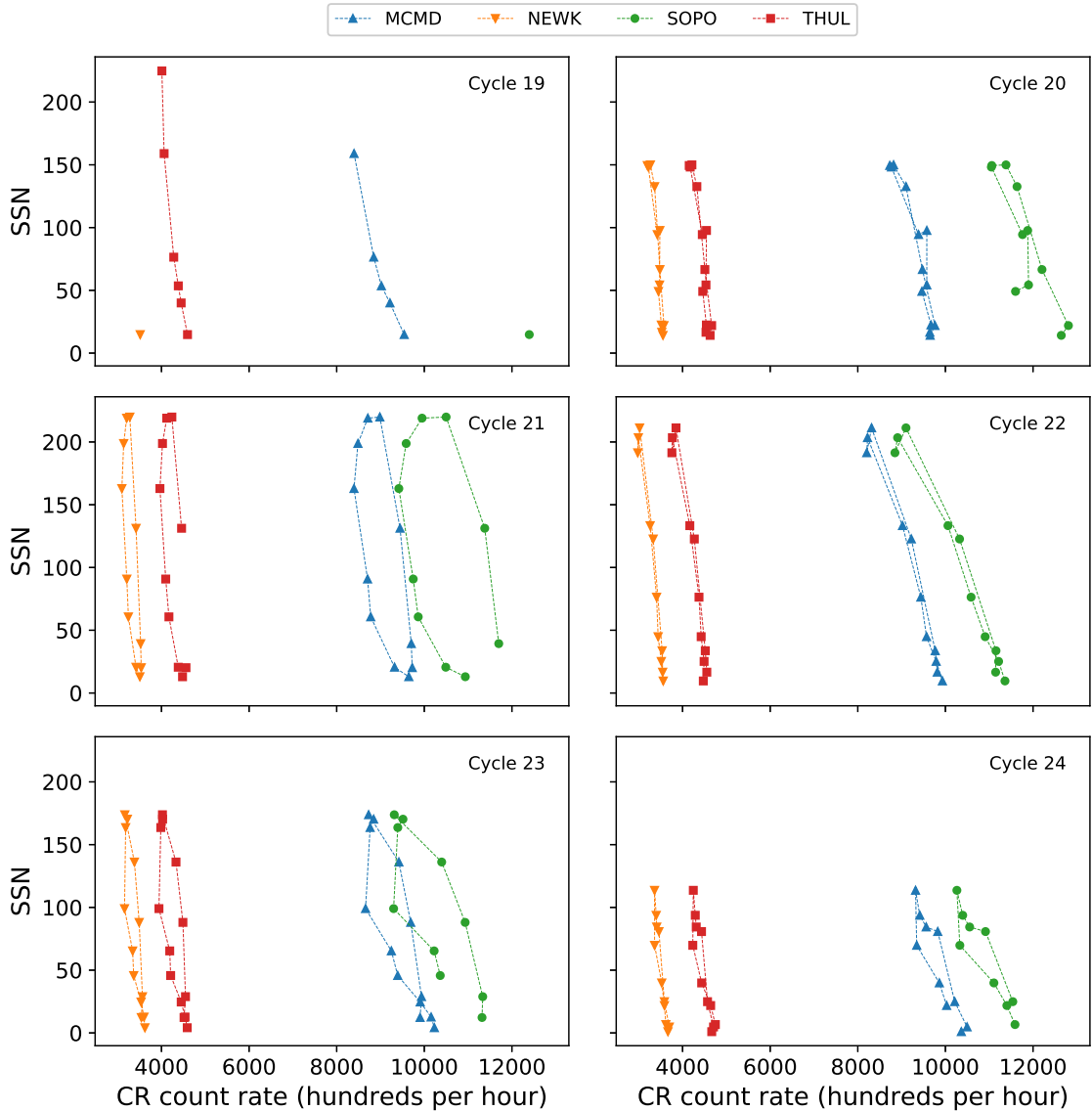


Figure 2.2: Hysteresis plots between yearly averaged SSN and yearly averaged GCR intensity for each of the 4 main NM stations over cycles 19-24.

showing that the even numbered solar activity cycles can be best modeled using a linear fit due to the narrow shape of the hysteresis loops; whereas odd-numbered solar activity cycles are better represented by ellipses due to their broader shape.

There has been speculation in the literature on the behaviour of cycle 24 compared to recent odd and even cycles. It has been suggested that there exists a lag between SSN maxima and GCR intensity minima in excess of 10 months (Kane, 2014; Mishra & Mishra, 2016) which does not follow the previous even cycles having a near-zero lag and in fact suggesting that cycle 24 behaved similarly to previous odd cycles; however these studies do not make use of a complete cycle of data and thus may draw inaccurate conclusions about the behaviour of the whole cycle because of the unusually extended nature of the declining phase of cycle 23 and the low amplitude of cycle 24 maximum (Broomhall, 2017). Mishra & Mishra (2016) make use of a more complete data set for cycle 24, yet still incomplete, and conclude that it is also likely that a 4 month lag could exist between GCRs and SSN.

This work aims to provide a timely update on the statistical relationship between GCR intensity and solar activity during solar cycle 24, since the cycle has now almost declined to a minimum. These aims have been achieved through a time-lag analysis and hysteresis effect analysis between SSN and GCR intensity.

In Section 2.2 we provide a brief description of the data that was used throughout this study for both CRs and SSN.

We show in Section 2.3 through a correlative time-lag analysis that there exists a small time-lag between the SSN and GCR intensity over solar cycle 24, which is slightly longer than preceding even-numbered cycles but not as high as observed in previous odd-numbered cycles. We also discuss whether the time-lag between SSN and GCR shows a dependence on the rigidity cut-off of the observing station.

In Section 2.4 we model the shapes of hysteresis plots between GCR intensity and SSN. We show that the behaviour of the hysteresis loops for cycle 24 follow the preceding even-numbered solar activity cycles and is better represented by a straight

line fit rather than an elliptical model.

## 2.2 Data

For the majority of the work in this study we have considered the pressure corrected count rates measured by four NM monitor stations as acquired from the NM data base (NMDB, 2018) event search tool (NEST) (<http://nmdb.eu/nest/>). The four stations are McMurdo (MCMD), Newark (NEWK), South Pole (SOPO), and Thule (THUL), i.e. the same NM stations used in the study by Inceoglu et al. (2014) to provide a comparison to existing literature. Table 2.1 details the basic characteristics of the NM stations used in this study.

We have investigated the long-term GCR modulation in the heliosphere from 1964-2018, spanning solar cycles 20-24, for the cycle epochs: 20: (10/1964 - 03/1976); 21: (03/1976 - 09/1986); 22: (09/1986 - 05/1996); 23: (05/1996 - 12/2008); 24: (12/2008 - 03/2018). Early predictions on solar cycle 25 suggest that solar cycle 24 is unlikely to reach a minimum earlier than the middle of 2019 up to as far as early 2021 (see Howe et al. (2018); Upton & Hathaway (2018); Pesnell & Schatten (2018)). The data used in this study are therefore of an incomplete cycle 24; however we believe this to now have a minimal effect on the results as cycle 24 draws to a minimum. Cycle 19 was omitted from this study due to the incomplete data set for this period (see Figure 2.1 and Figure 2.2).

During the time-lag correlation analysis, as our results suggested there may be a rigidity dependence on the time lag, we introduced a further 12 NM stations with data acquired from NEST spanning cycles 20-24 to increase the rigidity spectrum utilised in this study; these stations and their basic characteristics are also detailed in Table 2.1. These stations are not included in the rest of the results however as the results from these stations do not change the conclusions of this study.

Furthermore, we have also used monthly/yearly averaged SSN, as collected by WDC-SILSO (<http://sidc.be/silso/>), for the time-lag analysis/hysteresis anal-

Table 2.1: Neutron monitor stations used in this study and their vertical geomagnetic cut-off rigidity ( $R_c$ ), longitude, latitude, and altitude acquired from NEST. The first four stations have been used for all of the analysis while the lower 12 stations have been used exclusively for the investigation into the dependence of  $R_c$  on the time-lag.

	Station	$R_c$ [GV]	Long. [deg]	Lat. [deg]	$h$ [m]
Time-Lag & Hysteresis	McMurdo (MCMD)	0.30	166.6 E	77.9 S	48
	Newark (NEWK)	2.40	75.8 W	39.7 N	50
	South Pole (SOPO)	0.10	0.0 E	90.0 S	2820
	Thule (THUL)	0.30	68.7 W	76.5 N	26
$R_c$ dependence of time-lag	Oulu (OULU)	0.81	25.5 E	65.1 N	15
	Kerguelen (KERG)	1.14	70.3 E	49.4 S	33
	Magadan (MGDN)	2.10	151.1 E	60.0 N	220
	Climax (CLMX)	3.00	106.2 W	39.4 N	3400
	Dourbes (DRBS)	3.18	4.6 E	50.1 N	225
	IGY Jungfraujoch (JUNG)	4.49	7.98 E	46.6 N	3570
	Hermanus (HRMS)	4.58	19.2 E	34.4 S	26
	Alma-Ata B (AATB)	6.69	76.9 E	43.0 N	3340
	Potchefstroom (PTFM)	6.98	27.1 E	26.7 S	1351
	Mexico (MXCO)	8.28	99.2 W	19.8 N	2274
	Tsumeb (TSMB)	9.15	17.6 E	19.2 S	1240
	Huancayo (HUAN)	12.92	75.3 W	12.0 S	3400

ysis respectively as our chosen proxy of solar activity.

## 2.3 Time-Lag Analysis

### 2.3.1 Method

To investigate the time delay between the modulation of GCRs compared to the solar activity, a time-lag cross-correlation analysis was performed between monthly mean GCR intensity and monthly mean SSN for each station, following the approach of Usoskin et al. (1998). We used a time window of width  $T$  centred on a time  $t$ , i.e. shifting within the interval  $t - T/2$  to  $t + T/2$ . Here we used  $T = 50$  months.

The window was shifted in steps  $\Delta t = 1$  month within this interval and for each step the Spearman's rank correlation coefficient ( $\rho$ ) between GCR intensity and SSN was calculated. The lag between GCR and SSN was then estimated by finding the peak correlation coefficient within the time interval  $T$ .

The results from the four main NM stations used suggested that there may be a relationship between the rigidity cut-off ( $R_c$ ) of a NM station and the time-lag for GCRs; hence four additional NM stations were introduced to determine whether this was so, as detailed above.

### 2.3.2 Results

The correlation ( $\rho$ ) between monthly averaged GCR counts and SSN for different time-lags was calculated for cycles 20-23. The variation in  $\rho$  is presented in Figure 2.3, showing that for each cycle there is a time-lag corresponding to peak anti-correlation between GCR intensity and SSN. Table 2.2 summarises the time-lag with the highest correlation and the corresponding correlation coefficient for all stations in each individual solar cycle.

As previously reported in the literature, we see here that all of the NM stations clearly exhibit almost no lag during even solar cycles, and a longer lag varying between 11-21 months during odd solar cycles. There is a strong agreement between

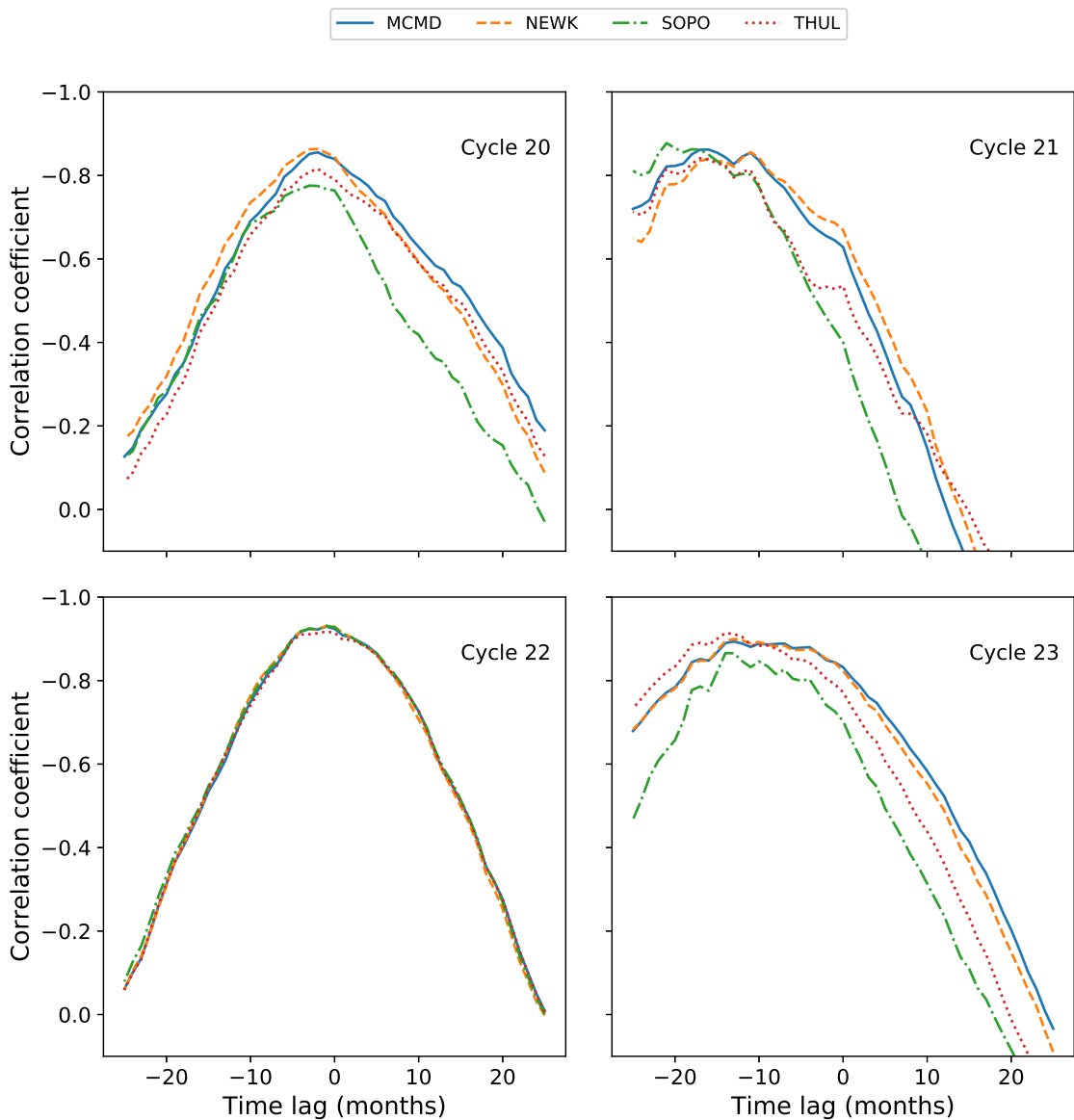


Figure 2.3: Variation in the correlation coefficient with time-lag NM station GCR intensity and SSN during solar cycles 20-23.

Table 2.2: Time-lags and the corresponding cross-correlation coefficient between NM CR count and SSN for solar cycles 20-23.

	Cycle 20		Cycle 21	
	Lag [months]	$\rho$	Lag [months]	$\rho$
McMurdo	2	-0.855	16	-0.862
Newark	2	-0.863	11	-0.856
South Pole	3	-0.776	21	-0.877
Thule	2	-0.816	17	-0.841
Cycle 22		Cycle 23		
	Lag [months]	$\rho$	Lag [months]	$\rho$
McMurdo	1	-0.929	13	-0.894
Newark	1	-0.931	13	-0.900
South Pole	1	-0.931	14	-0.866
Thule	1	-0.917	14	-0.914

the results presented in Table 2.2 and those of Mavromichalaki et al. (2007), Kane (2014), and Paouris et al. (2015), thus providing further evidence on the distinction between odd and even solar cycles due to particle transport in the heliosphere. The agreement with existing literature provides evidence of a suitable methodology in this study.

The same cross-correlation technique was then applied to cycle 24 between the dates 12/2008 - 03/2018 and the results are presented in Figure 2.4 and Table 2.3.

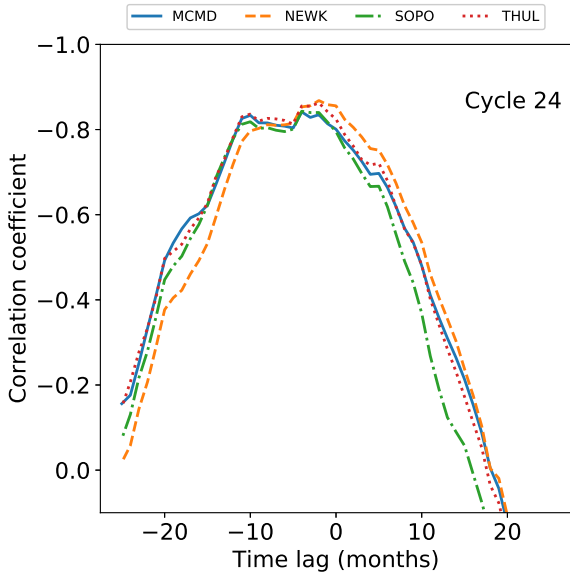


Figure 2.4: Variation in the correlation coefficient with time-lag between NM GCR intensity and SSN during solar cycle 24.

Table 2.3: Time-lags and the corresponding cross-correlation coefficient between NM GCR intensity and SSN for solar cycle 24.

Cycle 24		
	Lag [months]	$\rho$
MCMD	4	-0.841
NEWK	2	-0.868
SOPO	4	-0.843
THUL	2	-0.862

Cycle 24 is seen here to follow the pattern of almost no lag for even cycles; however cycle 24 does display a lag that is larger than the previous two even-numbered cycles, despite not being as large as the two previous odd-numbered cycles. The cause for the increased time-lag in cycle 24, as compared to the previous two even-numbered cycles, is likely due to the combined effects of the unusually deep and extended minimum between solar cycles 23 and 24, which delayed the decline in GCR intensity and caused record-breaking high GCR intensities (Pacini & Usoskin, 2015), and the small amplitude of the cycle 24 maximum.

The results presented in this study, using data for a near-complete cycle 24, show that the results of Kane (2014), and Mishra & Mishra (2016), were likely unduly influenced by the unusually deep and extended declining phase of cycle 23 given that they had a limited data set. Mishra & Mishra (2016) used data for just over half of cycle 24 and resulted in a time-lag of 4 months which agree with the results of this study.

As a further note on time-lag, Tomassetti et al. (2017) showed that through the introduction of time-lag as a parameter in the CR transport calculations of CR spectra that there exists a time-lag of  $8.1 \pm 1.2$  months during the period 2000-2012 spanning across cycle 23 and 24. We performed the time-lag analysis for the first 4 NM stations detailed in Table 2.1 for the period between 2000-2012 to investigate whether these results can be reproduced. The results of this analysis are presented in Figure 2.5 and Table 2.4.

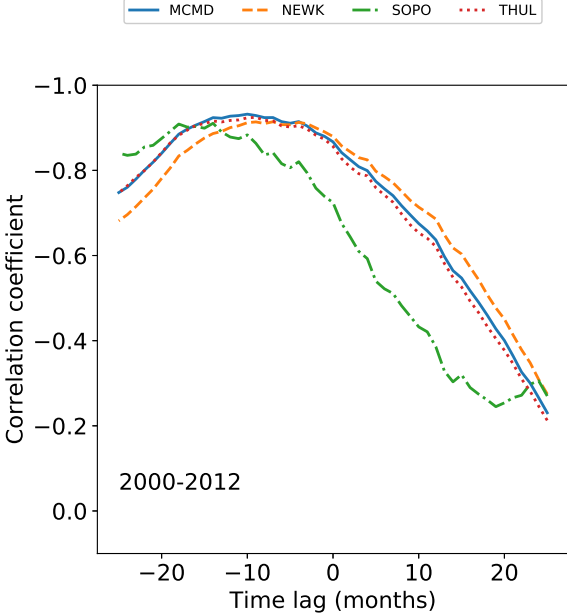


Figure 2.5: Variation in the correlation coefficient with time-lag between NM GCR intensity and SSN between 2000-2012.

From the time-lag analysis of the 4 stations presented there is a mean lag of  $10.00 \pm 1.47$  months, which is in good agreement with the results of Tomassetti et al. (2017).

Finally, allowing for the odd/even cycle dependence, we see in Figure 2.3, Figure 2.4, and Figure 2.5 that the time-lag appears to depend on the rigidity of the NM station used for observation. Such a dependence may impact the conclusions depending on the choice of NM station. We expect that if a dependence exists, a station with a higher rigidity cut-off ( $R_c$ ) would have a shorter lag as this station observes higher energy CRs which are affected less by solar modulation and thus able to recover faster from solar maximum. Whereas a station with a lower cut-off rigidity observing lower energy CRs, which are more influenced by solar modulation, would recover more slowly from solar modulation and therefore experience a longer time-lag. This is supported by Figure 2.3, Figure 2.4, and Figure 2.5, but in order to provide more conclusive evidence of such a relationship we introduced the additional NM stations detailed in Table 2.1 to provide a rigidity range spanning 0-13 GV. We present in Figure 2.6 a plot of the time-lag versus station  $R_c$  for all

Table 2.4: Time-lags and the corresponding cross-correlation coefficient between NM GCR intensity and SSN during 2000-2012.

2000-2012		
	Lag	$\rho$
	[months]	
MCMD	10	-0.932
NEWK	7	-0.914
SOPO	14	-0.911
THUL	9	-0.925

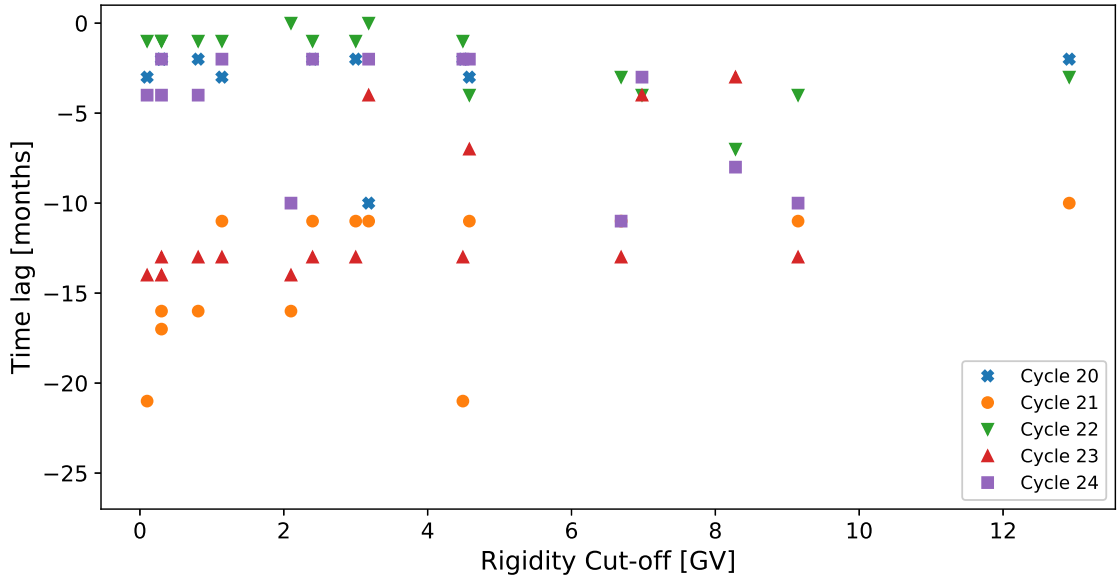


Figure 2.6: Variation in time-lag plotted against NM station rigidity cut-off for the 16 NM stations detailed in Table 2.1.

16 stations over cycles 20-24. To acquire uncertainties on the time-lag we ran 1000 Monte Carlo simulations of the time-lag analysis, sampling from the uncertainty distributions for each of the monthly averaged SSN and GCR counts; however the uncertainties in the data propagated in the Monte Carlo simulations produced no scatter in the overall results.

The results of this analysis do not show a clear rigidity dependence on the time-lag between SSN and GCR intensity; the sampling of higher  $R_c$  is too low, due to the availability of high  $R_c$  stations, to reasonably conclude on such a dependence at high rigidities, despite cycle 21 suggesting the existence of a dependence for low  $R_c$  stations as per our expectations. For low  $R_c$  stations there appears to be a more pronounced distinction between the time-lag observed between odd-numbered and even-numbered cycles than for higher  $R_c$  stations, however again this is not definitive due to the low sampling at higher  $R_c$ . We therefore conclude that there will be no significant dependence of the time-lag analysis on the  $R_c$  of the observing station.

## 2.4 Hysteresis Effect Analysis

### 2.4.1 Method

To investigate the hysteresis effect, we have adopted the approaches of Van Allen (2000), Singh et al. (2008), and Inceoglu et al. (2014). Plots of the annual mean SSN versus the annual mean GCR intensity were generated for cycle 20-24 and analysed by fitting different models to the data.

As highlighted in Inceoglu et al. (2014), even-numbered solar cycles can be suitably modeled by a linear fit due to their narrow hysteresis shape, and odd-numbered solar cycles were shown to be better modeled by ellipses due to their broadened hysteresis shape. Here, we first repeated for solar cycles 20-23 the linear and ellipse fitting to confirm the method reproduces the results reported in Inceoglu et al. (2014) before applying the method to cycle 24.

For even cycles which display narrow hysteresis loops, an unweighted least squares linear regression was used to reconstruct estimates of the GCR intensity from SSN. As odd-numbered solar cycles display a broader hysteresis loop, they were separately modeled using unweighted linear regression and ellipse fitting to determine the model providing the better fit.

The equation of the ellipse fitting took the form:

$$\begin{bmatrix} x \\ y \end{bmatrix} = \begin{bmatrix} x_0 \\ y_0 \end{bmatrix} + R(\phi) \begin{bmatrix} a \cos \theta \\ b \sin \theta \end{bmatrix} \quad (2.1)$$

where  $x$  is GCR intensity;  $y$  is SSN;  $(x_0, y_0)$  are the centroid coordinates of the fitted ellipse,  $R(\phi)$  is the rotation matrix;  $\phi$  is the ellipse tilt angle;  $a$  and  $b$  are the semi-major and semi-minor axes respectively; and  $0 \leq \theta \leq 2\pi$  is the polar angle measured anti-clockwise from the semi-major axis.

In order to regain the GCR intensity from the model, where linear regression was used to model the data, GCR was acquired directly from the SSN for each year.

For the ellipse model the GCR was acquired from the model as a function of time from  $\theta$ , where the time-lag calculated from the analysis in Section 2.3 was used to correctly phase the ellipse allowing  $\theta$  to be calculated using standard equations of ellipses.

GCR intensity predicted by the linear regression and ellipse models were compared to the measured GCR intensity using Spearman's rank correlation as per Inceoglu et al. (2014).

### 2.4.2 Results

The hysteresis loops between yearly averaged SSN and GCR intensity for each station were first modeled with a linear regression for both odd and even solar activity cycles, then the odd cycles were separately re-modeled by ellipse fitting to show that this provides a more representative fit as suggested in Inceoglu et al. (2014). The correlation between measured CR intensities and modeled CR intensities for cycles 20-23 are presented in Table 2.5.

Table 2.5: Correlation coefficients of the linear regression and ellipse modeling of the hysteresis plots for solar cycles 20-23.

	Cycle 20		Cycle 21		Cycle 22		Cycle 23	
	Linear	Ellipse	Linear	Ellipse	Linear	Ellipse	Linear	Ellipse
McMurdo	0.867	-	0.664	0.946	0.964	-	0.846	0.852
Newark	0.888	-	0.700	0.964	0.955	-	0.857	0.874
South Pole	0.746	-	0.358	0.939	0.936	-	0.733	0.855
Thule	0.783	-	0.912	0.964	0.900	-	0.813	0.929

There is a consistent and good agreement between the measured and modeled CR intensities for even solar cycles modeled through linear regression, because the hysteresis loops are quite narrow as shown in Figure 2.7. These results support the findings of Inceoglu et al. (2014). Note that discrepancies in the correlation coefficients between this study and Inceoglu et al. (2014) are likely due to a number of reasons: Inceoglu et al. (2014) used data smoothing processes where in this study raw data are used; Inceoglu et al. (2014) made use of monthly mean data, whereas

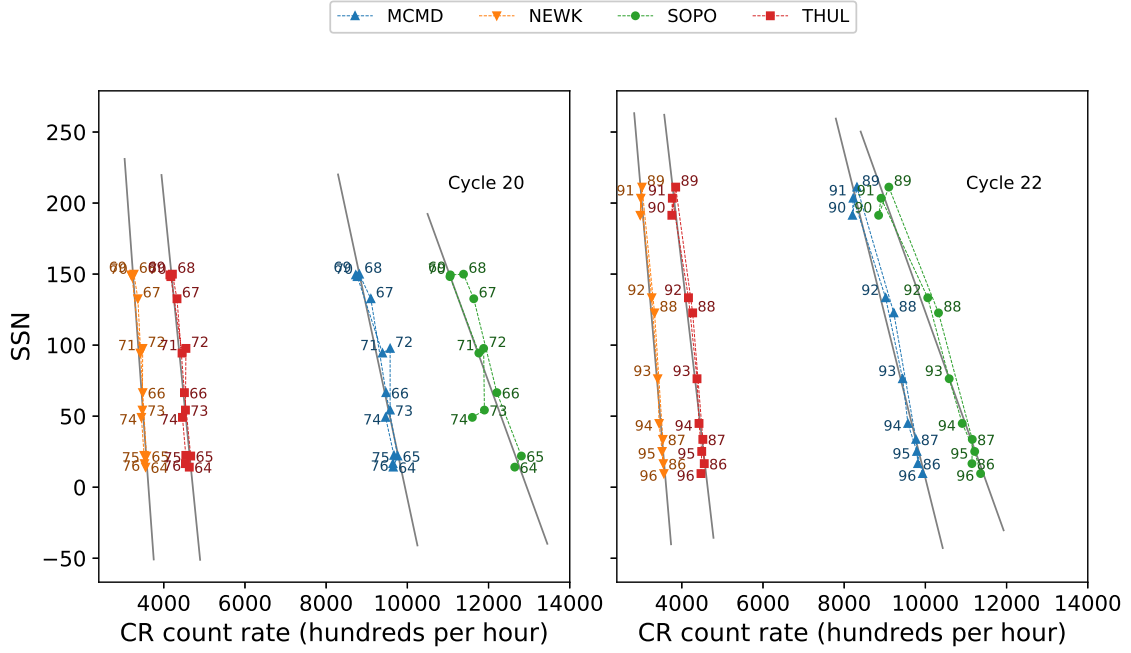


Figure 2.7: The hysteresis plots for even solar cycles 20 and 22 and the linear regression fit to the data.

annual mean data was used in this study; Inceoglu et al. (2014) interpolated missing data, whereas gaps have been left untreated in this study.

The linear relations for odd solar cycles are less consistent in their agreement with observed CR intensities, with the correlation during cycle 21 as low as 0.34 for South Pole and as high as 0.91 for Thule. Across both of the odd cycles considered in this study linear regression is not as good a representation of the data as for even cycles. Figure 2.8 shows the wider hysteresis loops which is a characteristic of odd solar cycles and shows visually that a linear fit does not provide a good representation of the data.

In agreement with the results of Inceoglu et al. (2014), it can be seen from the results in Table 2.5 that the ellipse models provide estimates of the CR intensity which are in good agreement with the measured intensities due to the increased correlation coefficient for each station during cycle 21 and cycle 23; for SOPO during cycle 21 the increase in  $\rho$  is seen to be 0.58 proving the benefit of the ellipse model.

If cycle 24 follows the pattern between odd and even cycles, it is expected that

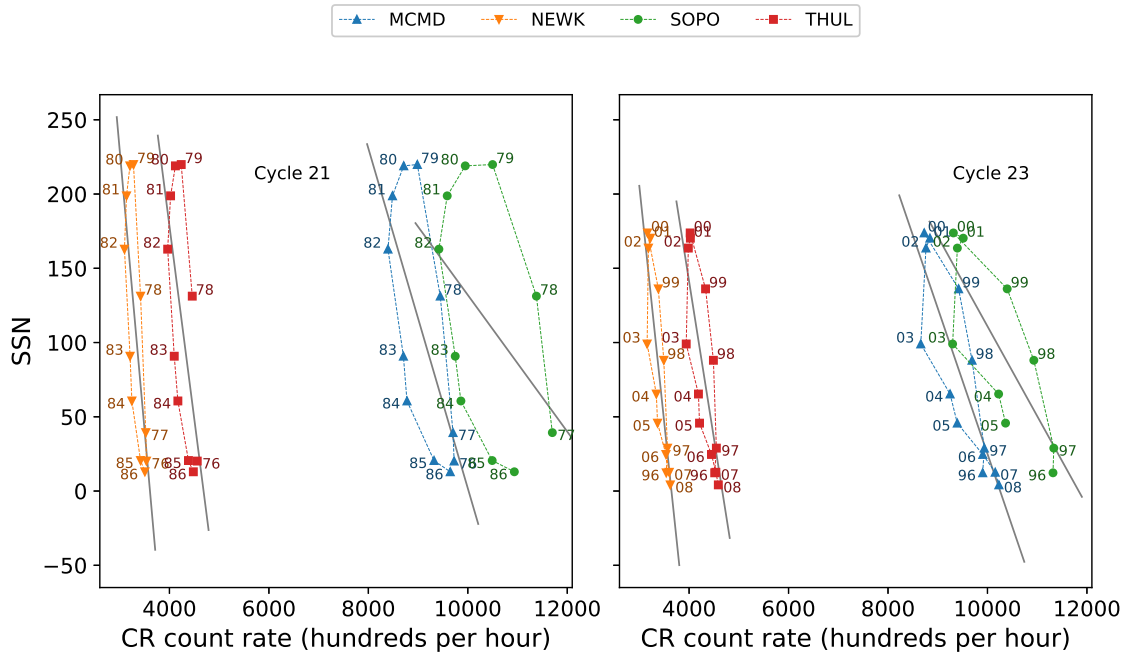


Figure 2.8: The hysteresis plots for odd solar cycles 21 and 23 and the linear regression fit to the data.

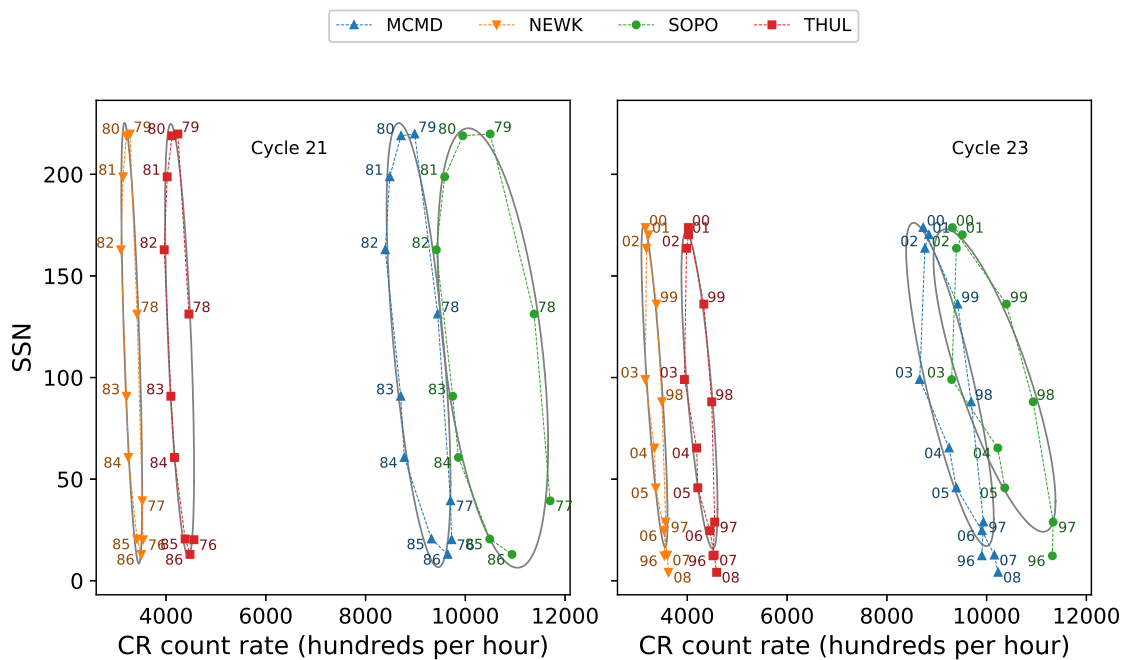


Figure 2.9: The hysteresis plots for odd solar cycles 21 and 23 and the ellipse fit to the data.

the best fit will be provided by the linear model; however it can be seen in Figure 2.2 that cycle 24 appears to display a wider hysteresis loop than the two preceding even-numbered cycles. Both the linear model and ellipse model were applied to the hysteresis plots for solar cycle 24 to determine which model would provide the better fit; the correlation between measured CR intensities and modeled CR intensities are presented in table 2.6.

Table 2.6: Correlation coefficients of the linear regression and ellipse modeling of the hysteresis plots for solar cycle 24.

	Cycle 24	
	Linear	Ellipse
McMurdo	0.903	0.927
Newark	0.936	-
South Pole	0.883	-
Thule	0.873	0.936

The linear model for cycle 24 shows a good correlation between the observed and modeled CR intensities providing evidence to suggest that cycle 24 follows the two preceding even-numbered cycles. The ellipse model does however improve the relation between the observed and modeled CR intensities for 2 out of the 4 stations: McMurdo and Thule. For South Pole and Newark the ellipse model was not able to provide a fit at all, which is believed to be due to the Newark data points crossing where the semi-major axis would be defined for the ellipse model causing the calculation of the semi-major and semi-minor axes to return as not a number, and the South Pole has data missing at the beginning of cycle 24.

The results for solar cycle 24 do not provide a conclusive answer as to whether cycle 24 behaves like past even solar cycles or odd cycles from this data set alone; however the ellipse model does not provide as significant an improvement for the two modeled NM stations as for odd cycles. The small improvement in the ellipse fit is likely due again to the effects of the extended declining phase of cycle 23 and the unusually low activity of cycle 24.

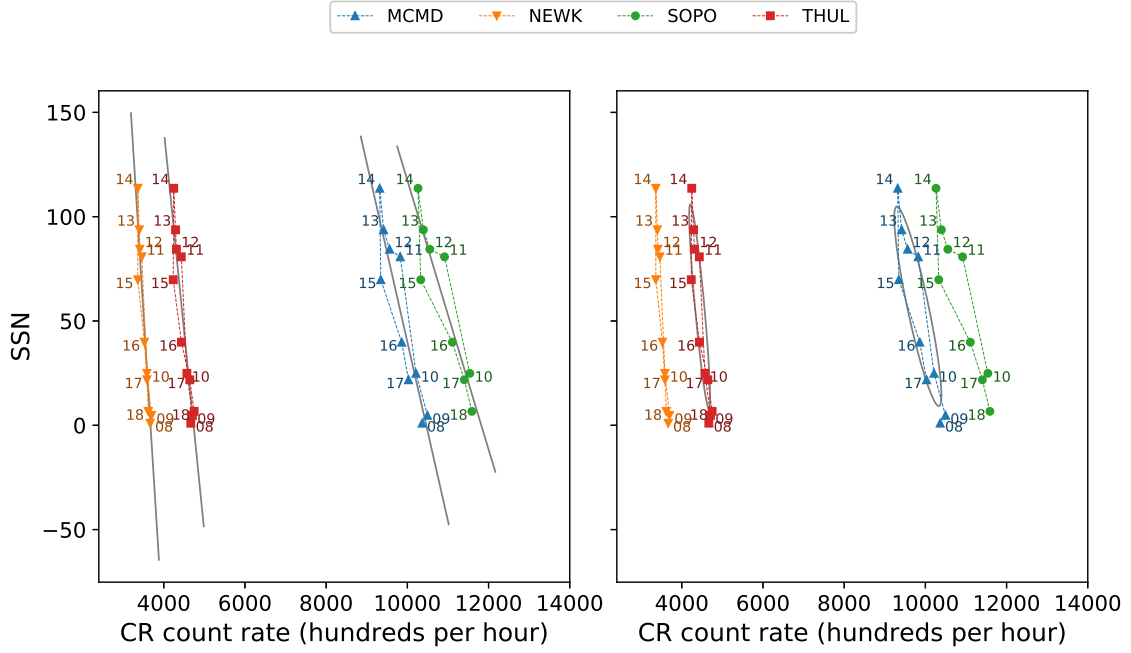


Figure 2.10: The hysteresis plot for solar cycle 24, and the linear regression fit to the data (left) and ellipse fit to the data (right).

We repeated the analysis for the additional 4 NM stations that featured in this study. Again, the linear model provided a good fit to the data however the ellipse model was not able to provide a fit; favouring the conclusion that cycle 24 is best represented by a simple linear model as was true for the preceding even-numbered cycles.

Despite cycle 24 having not yet declined to a minimum, it is clear from the observations shown in the hysteresis plots that further data in cycle 24 is unlikely to broaden the loop any further. The hysteresis loop begins to tighten up after 2016 following the broadening between 2014-2016; hence it appears unlikely that by the end of cycle 24 further observations will support the ellipse model and instead will favour the linear fit to the data.

## 2.5 Conclusions

As cosmic rays are modulated by the heliosphere during the 11-year solar activity cycle, and this effect has been studied for previous solar cycles, the principal aim of

this study was to investigate the nature of GCRs during the current activity cycle 24 as it draws to a minimum.

In this study we presented a time-lag analysis between GCR intensity and SSN which showed that cycle 24 has a longer lag (2-4 months) than the preceding even-numbered solar activity cycles (typically 0-1 months); however its lag is not as large as preceding odd-numbered cycles, and cycle 24 follows the trend of a short or near-zero lag for even-numbered cycles. We suggest here that the cause of the extended lag in cycle 24 compared to previous even-numbered cycles is likely due to the deep, extended minimum between cycle 23 and 24, and the low maximum activity of cycle 24 (Broomhall, 2017).

It has been previously shown in the literature that there is a striking difference in the shape of the plot of SSN and GCR intensity between odd-numbered and even-numbered solar cycles. Due to the difference in the shape of the hysteresis plots for odd-numbered and even-numbered cycles, we have modeled the hysteresis plots using both a simple linear model and an ellipse model. The results of this study tend to support that cycle 24 follows the same trend as preceding even-numbered cycles and is best represented by a straight line rather than an ellipse, such is the case for odd-numbered activity cycles.

We emphasise that although cycle 24 has not yet ended, the shape of the hysteresis plots suggest that we are now past the main broadening region and the inclusion of further data for cycle 24 will very likely only support the linear model. This study will continue to follow the evolution of the cycle 24 until the onset of cycle 25, in around 2019-2021 (Howe et al., 2018; Upton & Hathaway, 2018; Pesnell & Schatten, 2018), when an update on the final results of cycle 24 should be provided.

## 2.6 Update: End of Cycle 24

## 2.7 Comparison with HiSPARC

The analysis was repeated using data from HiSPARC station 501, over the period between 2008 – 2019, to investigate whether the HiSPARC (HS) network was capable of monitoring the solar cycle variation in the muon count rate. HiSPARC station 501 is the best candidate for this analysis due to its long operational lifetime, in comparison to other HS stations, which spans most of cycle 24, and due to the fact that this station is used as the *gold standard* HS station.

This was further motivated by the observations of Fan & Velthuis (2018), in which they stated a confirmation of the accepted anti-correlation between solar activity and CRs after analysing the count rate of the HS 501 station, comparing the count rate with the number of solar flares and the SSN during the rising phase of cycle 24.

We also wanted to determine whether the results of the analysis for the behaviour of CRs during cycle 24, using HS data, agreed with those acquired above, using NM data.

A plot of the HS 501 data over this period is given in Figure 2.11, which shows a comparison between the HS count rate and SSN. By-eye, no clear anti-correlation is displayed between the HS count rate and the SSN.

The spearman correlation coefficient between the HS count rate and the SSN was calculated between the two data sets, without performing the time-lag analysis, to be,  $\rho = 0.078$ . It was quantitatively concluded therefore that there exists no correlation between the SSN and the HS muon count rate, confirming what was suspected by-eye.

This lack of anti-correlation is, unfortunately, symptomatic of the set-up of the HS stations. There exists a stand-out reason why the set-up of the HS stations limits the capability of HS to observe the solar cycle modulation of CR intensity,

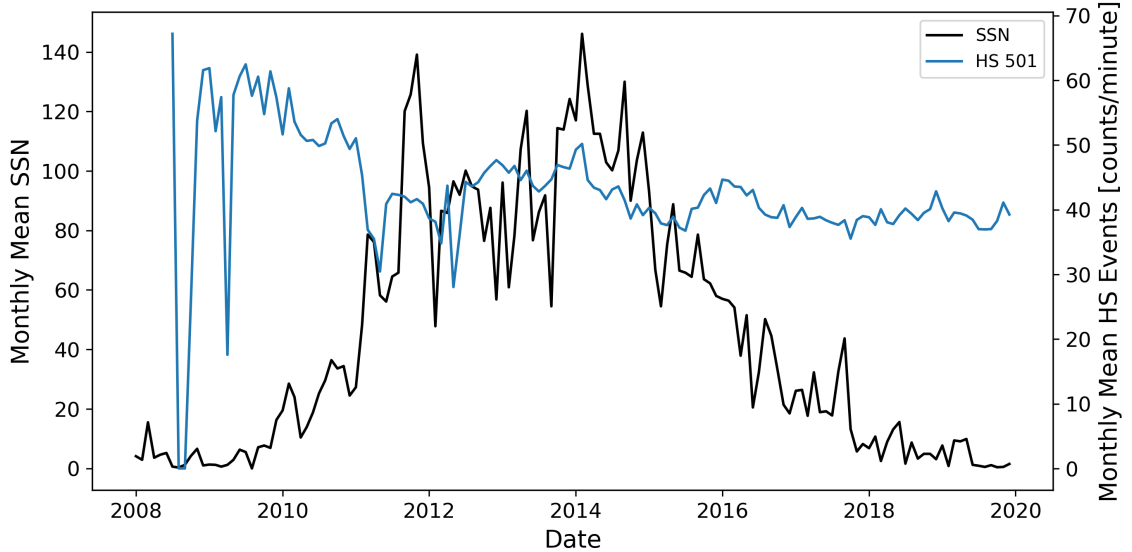


Figure 2.11: The monthly-mean CR-induced muon count rate recorded by HiSPARC (blue), and the SSN (black) between 2008 – 2019.

tweaking of the detector threshold setting.

The HiSPARC stations are typically set up to achieve a singles rate of around 100 Hz above the higher threshold limit, resulting in an events rate of around 1 Hz for the station. The PMT is often adjusted when the count rate strays away from the nominal value, and this mitigates the ability of HiSPARC to reliably observe the solar cycle variation.

Modifications to the PMT voltage of each detector in HS 501 is illustrated in Figure 2.12, and shows the scale of the adjustments, with the voltages varying by as much as  $\sim 80$  V. The effect of varying the PMT voltage is dependent on the individual PMT, but a change of 50–100 V will have an effect on the count rate, therefore it is likely to be a root cause for not observing the solar cycle modulation.

The claim that the solar cycle variation was observed in the count rate of HS 501 data by Fan & Velthuis (2018) was highly likely based on their limited data set, spanning not enough of solar cycle 24. One could be convinced from the count rate during the rising phase of cycle 24 that the cycle variation is observed...

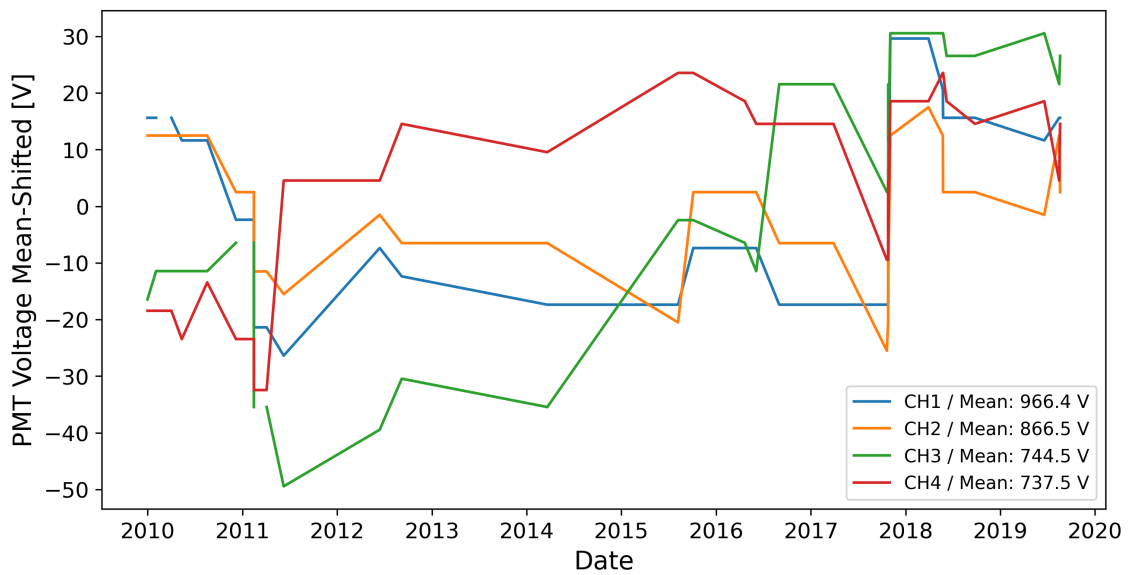


Figure 2.12

# Bibliography

- Aab A., et al., 2017, Science, 357, 1266
- Aslam O. P. M., Badruddin 2012, Solar Physics, 279, 269
- Aslam O. P. M., Badruddin 2015, Sol Phys, 290, 2333
- Belov A., 2000, Space Science Reviews, 93, 79
- Berkova M. D., Belov A. V., Eroshenko E. A., Yanke V. G., 2011, Bull. Russ. Acad. Sci. Phys., 75, 820
- Broomhall A.-M., 2017, Sol Phys, 292, 67
- Desorgher L., Flckiger E. O., Gurtner M., 2006. p. 2361, <http://adsabs.harvard.edu/abs/2006cosp...36.2361D>
- Dunai T. J., 2010, in , Cosmogenic Nuclides: Principles, Concepts and Applications in the Earth Surface Sciences. Cambridge University Press, Cambridge, pp 1–24, doi:10.1017/CBO9780511804519.003, /core/books/cosmogenic-nuclides/cosmogenic-nuclides/F85F29AC333CD6F7C9CE2B9155B43B13
- Fan K.-z., Velthuis J., 2018
- Forbush S. E., 1958, Journal of Geophysical Research, 63, 651
- Giacalone J., 2010, in Schrijver C. J., Siscoe G. L., eds, , Heliophysics: Space Storms and Radiation: Causes and Effects. Cambridge University Press, Cambridge, pp 233–262, doi:10.1017/CBO9781139194532.010, /core/books/heliophysics-space-storms-and-radiation-causes-and-effects/energetic-particle-transport/FC3869AB4D484479501B015DCB07A976
- Heck D., Pierog T., 2017, Technical Report 7.6400, Extensive Air Shower Simulation with CORSIKA: A Users Guide
- Herbst K., Kopp A., Heber B., 2013, Annales Geophysicae, 31, 1637
- Howe R., Hill F., Komm R., Chaplin W. J., Elsworth Y., Davies G. R., Schou J., Thompson M. J., 2018, ApJL, 862, L5
- Inceoglu F., Knudsen M. F., Karoff C., Olsen J., 2014, Sol Phys, 289, 1387
- Janardhan P., Fujiki K., Ingale M., Bisoi S. K., Rout D., 2018, Astronomy and Astrophysics, 618, A148

- Kane R. P., 2014, Solar Physics, 289, 2727
- Mavromichalaki H., Paouris E., Karalidi T., 2007, Sol Phys, 245, 369
- Mendon{\c{c}}a R. R. S. d., et al., 2016, ApJ, 830, 88
- Mishra V. K., Mishra A. P., 2016, Indian J Phys, 90, 1333
- NMDB 2018, NMDB Event Search Tool (NEST), <http://www.nmdb.eu/nest/>
- Owens M. J., Forsyth R. J., 2013, Living Rev. Sol. Phys., 10, 5
- Pacini A. A., Usoskin I. G., 2015, Sol Phys, 290, 943
- Paouris E., Mavromichalaki H., Belov A., Eroshenko E., Gushchina R., 2015, J. Phys.: Conf. Ser., 632, 012074
- Parker E. N., 1965, Planetary and Space Science, 13, 9
- Paschalis P., Mavromichalaki H., Yanke V., Belov A., Eroshenko E., Gerontidou M., Koutroumpi I., 2013, New Astronomy, 19, 10
- Pesnell W. D., Schatten K. H., 2018, Sol Phys, 293, 112
- Ross E., Chaplin W. J., 2019, Sol Phys, 294, 8
- Savi M., Maleti D., Jokovi D., Veselinovi N., Banjanac R., Udovii V., Dragi A., 2015, J. Phys.: Conf. Ser., 632, 012059
- Singh M., Singh Y. P., Badruddin 2008, Journal of Atmospheric and Solar-Terrestrial Physics, 70, 169
- Thomas S. R., Owens M. J., Lockwood M., 2014a, Sol Phys, 289, 407
- Thomas S. R., Owens M. J., Lockwood M., Scott C. J., 2014b, Solar Physics; Dordrecht, 289, 2653
- Tomassetti N., Orcinha M., Baro F., Bertucci B., 2017, ApJL, 849, L32
- Upton L. A., Hathaway D. H., 2018, Geophysical Research Letters
- Usoskin I. G., Kananen H., Mursula K., Tanskanen P., Kovaltsov G. A., 1998, Journal of Geophysical Research: Space Physics, 103, 9567
- Van Allen J. A., 2000, Geophysical Research Letters, 27, 2453